A Narrow-Linewidth Laser at 1550 nm Using the Pound-Drever-Hall Stabilization Technique

Evan M. Lally

Thesis submitted to the Faculty of the

Virginia Polytechnic Institute and State University

in partial fulfillment of the requirements for the degree of

Master of Science

in

Electrical Engineering

Dr. Anbo Wang, Chair

Dr. Gary S. Brown

Dr. Ahmad Safaai-Jazi

Dr. Randy Heflin

August 11, 2006

Blacksburg, Virginia

A Narrow-Linewidth Laser at 1550 nm Using the Pound-Drever-Hall Stabilization Technique

Evan M. Lally

Center for Photonics Technology

Virginia Tech

(ABSTRACT)

Linewidth is a measure of the frequency stability of any kind of oscillator, and it is a defining characteristic of coherent lasers. Narrow linewidth laser technology, particularly in the field of fiber-based infrared lasers, has progressed to the point where highly stable sources are commercially available with linewidths on the order of 1-100 kHz. In order to achieve a higher level of stability, the laser must be augmented by an external frequency stabilization system.

This paper presents the design and operation of a frequency locking system for infrared fiber lasers. Using the Pound-Drever-Hall technique, the system significantly reduces the linewidth of an input laser with an un-stabilized linewidth of 2 kHz. It uses a high-finesse Fabry-Perot cavity, which is mechanically and thermally isolated, as a frequency reference to measure the time-varying frequency of the input laser. An electronic feedback loop works to correct the frequency error and maintain constant optical power. Testing has proven the Pound-Drever-Hall system to be highly stable and capable of operating continuously for several seconds at a time.

DEDICATION

This work is dedicated to my wife, Lindsay. Thank you for all of your love and steadfast support. You are the center of my life.

ACKNOWLEDGMENTS

I would like to thank my advisor, Professor Anbo Wang, for giving me the freedom and the tools to pursue this project, and for the guidance and advice that helped make it work. Thank you for sharing your patience, encouragement and expertise, and for giving me such a tremendous opportunity.

I owe a great deal of thanks to Dr. Jim Bergquist and the Ion Storage Group at NIST, Boulder. Thank you for generously sharing your time and your home, allowing me to visit and see your incredible work. By allowing us to learn from your system and borrow your Fabry-Perot etalon design, you put us on the path to success. Your help has been simply indispensable.

Debbie Collins, our grants administrator, has been instrumental in keeping this project organized and providing behind-the-scenes support. Thank you, Debbie for all of your help.

The strength of any lab lies in its students and staff, and without my colleagues at the CPT, none of this work would have been possible. I would especially like to thank Dr. Xiaopei Chen, Bo Dong, Dr. Ming Han, Dr. Fabin Shen, Yongxin Wang, and Yizheng Zhu. Independently, each of you is an exceptional scientist and engineer, but together, the sum of your knowledge is truly powerful. Thank you for all of your help.

Finally, I would like to thank the members of my committee, Professors Gary Brown, Randy Heflin, and Ahmad Safaai-Jazi, for all of their help, support, and comments.

CONTENTS

LIST OF FIGURES

LIST OF TABLES

1. INTRODUCTION

The ability of lasers to produce phase-coherent light lies at the heart of almost every optical device. The ideal laser produces a perfectly coherent color, a single frequency. Like all oscillators, however, the coherence of any real laser source is relative. There is always a certain amount of phase, or frequency noise in the laser output, and this noise produces a broadened frequency spectrum. The measurement of this spectral width is the laser's linewidth, and commercially available lasers can have linewidths ranging from several kHz to several GHz.

Through the use of a stabilized feedback system, it is possible to lock the frequency of an ordinary laser so that its frequency noise is reduced to a negligible level. The optical phase locking technique developed by Pound, Drever and Hall [1] is widely accepted as the best method of laser frequency stabilization, and it has been successfully demonstrated on lasers of various wavelengths. Most modern Pound-Drever-Hall (PDH) systems have been built using visible and near-IR lasers (with wavelengths from 400 to 1064 nm) for the purpose of molecular spectroscopy experiments. The scientists at NIST, Boulder have successfully used the PDH technique to lock a 563 nm dye laser, reducing its linewidth to less than 0.16 Hz [2].

Although several ultra-narrow linewidth lasers already exist at visible wavelengths, a frequency-stabilized infrared laser would offer new possibilities in precision sensing and measurement. Infrared lasers, particularly those with a wavelength of 1550 nm, lend themselves

quite well to all kinds of optical fiber-based experiments because the vast majority of modern optical communications and sensing equipment is designed for this wavelength. A narrow-linewidth laser at 1550 nm could be used to calibrate precision fiber-based sensors, filters and multiplexers. It could be used in conjunction with these highly sensitive optical devices to make precision measurements of physical phenomena. Used as a kind of frequency reference, a narrow-linewidth infrared laser could aide in the difficult process of measuring the spectral width of other narrowband lasers.

Based on work done by Dr. Jim Bergquist and the Ion Storage Group at NIST, Boulder, this project demonstrates the feasibility and basic operation of a stabilized 1550 nm narrow-linewidth laser. This PDH frequency locking system has been shown to significantly reduce the spectral width of the input laser. The output of the stabilized laser is a highly stable continuous-wave frequency reference capable of generating 1 mW output power for a duration of several seconds. Future plans for the project include improvements to further narrow the output linewidth, construction of a device to more exactly measure the resulting spectral width, and precision measurement and calibration experiments using the stabilized laser system.

2. BACKGROUND

2.1 Context: Frequency Standards

Frequency standards often come in two pieces: a component with high short-term stability, and a long-term stable reference. Generally speaking, these two attributes are mutually exclusive. Linewidth is a measure of short-term stability, and oscillators with a narrow linewidth tend to drift over a period of hours or days. Conversely, a reference with zero-mean long-term drift usually does not have a very narrow short-term linewidth. From commercial GPS standards to microwave and optical atomic clocks, any complete frequency standard uses a narrow linewidth oscillator as its output, but also uses averaging to check its frequency against a long-term stable reference [3].

In this context, the Pound-Drever-Hall (PDH) frequency locking system produces one half of an absolute frequency reference. Standards laboratories around the world use this technique to produce coherent lasers with very narrow linewidths, and then they reference the stabilized laser to an atomic transition with a somewhat larger intrinsic linewidth [4]. These optical standards are the recent trend in precision frequency metrology because optical clocks have inherently higher potential than their microwave counterparts. The high frequency of light (100-1000 THz) provides a much finer "ruler" with which to measure time [5].

Due to the wide range of available atomic transitions, the PDH technique has been successfully demonstrated at several wavelengths. Overall, the narrowest published laser

linewidth was achieved by the Ion Storage Group at NIST, who reduced the linewidth of a 563 nm dye laser to only 0.16 Hz [2]. Scientists at the National Physics Laboratory (U.K) have recently demonstrated a ND:YAG laser (1064 nm) with a 0.46 Hz linewidth using the same technique [6]. Clearly, the PDH method works well and is adaptable to almost any wavelength.

One of the main advantages to the PDH technique that it prevents laser intensity noise from coupling directly into the frequency error signal. Prior to the establishment of this method, frequency locking systems utilizing a Fabry-Perot etalon as a frequency discriminator were required to use a derivative technique [7]. This derivation was performed electronically, and the technique required that the transmission through the etalon be measured as well as the reflected signal.

Efforts to lock communication wavelength lasers (1530-1550 nm) to Fabry-Perot resonances have been focused on building Acetylene (C_2H_2) atomic clocks [8, 9]. In these systems, a laser with active Erbium-doped glass gain medium is stabilized to a linewidth on the order of 50 kHz by the PDH method. The relatively large linewidth can be explained by the low initial stability of the tunable bulk optics lasers, and the width of the C_2H_2 absorption line. Acetylene has several resonances in this region with a minimum enhanced linewidth of 1 MHz, so there is little need to reduce the probe laser linewidth to below the kHz level.

2.2   Motivation and Applications

The vast majority of PDH systems were built in an effort to produce two-stage absolute frequency references (atomic clocks). These efforts limited the wavelengths of interest to the visible and near-infrared ranges, where most of the narrow atomic absorption lines occur.

However, fiber-based communication lasers at 1550 nm provide an attractive new basis for a narrow linewidth system. These lasers use an erbium-doped optical fiber as the gain element, and Fiber Bragg Gratings (FBGs) to define the lasing cavity [10]. They are remarkably stable, with linewidths on the order of one kHz, so they offer a much better starting point for frequency stabilization.

Applied to a narrow linewidth fiber laser, the PDH technique has the potential to produce light with incredibly high short-term frequency stability. Availability of high-quality communications equipment, such as fiber amplifiers, switches, and modulators, makes the possibility of an ultra-stable 1550 nm source particularly attractive for applications not requiring an absolute frequency reference. Any application involving heterodyne detection, such as sensor demodulation and characterization, DWDM communication systems, and measurement of fundamental physical constants, is an ideal usage for such a laser.

Laser linewidth measurement is an area that presents both a challenge and an important application for the 1550 nm PDH lock project. Currently, the best technique for laser linewidth measurement is Delayed Self-Heterodyne Interferometry (DSHI), in which the laser light is sent into a Mach-Zender interferometer with one very short path and another path longer that the coherence length of the laser. Under these conditions, the beat note at the interferometer output is produced by two uncorrelated signals, and the spectral width of this note is equal to twice the input laser linewidth. The drawback to this technique is that, for narrow linewidth lasers, the coherence length is extremely long, and thermal and acoustic perturbations along the long path can introduce additional phase noise, obscuring the true laser linewidth.

The ultra-narrow linewidth laser system provides a convenient reference through which even highly stable lasers can be characterized by comparison. Used in this way, the PDH lock eliminates the need for a cumbersome Mach-Zender interferometer; the laser under test

must simply beat with the stabilized source, and the linewidth can be directly inferred from the beat note.

The inherent challenge is that the stabilized linewidth of the PDH system is very difficult to measure. The coherence length of this source is far too long for the DSHI technique, so the only way to definitively measure the linewidth is to build two statistically independent PDH systems [11]. Exact linewidth measurement is beyond the scope of this project, but this paper does present a linewidth estimation by sub-coherence length DSHI method.

3. POUND-DREVER-HALL THEORY

The Pound-Drever-Hall (PDH) laser frequency stabilization technique is essentially a frequency-locking feedback loop. An incoming laser with a moderate amount of frequency jitter is incident on a Fabry-Perot etalon, which serves as a frequency reference. The reflected signal is proportional to the instantaneous frequency error, as measured with respect to the etalon's stable resonant frequency. This error signal is then processed by analog electronics and fed back to an optical frequency shifter, which adjusts the incoming laser frequency to eliminate the error.
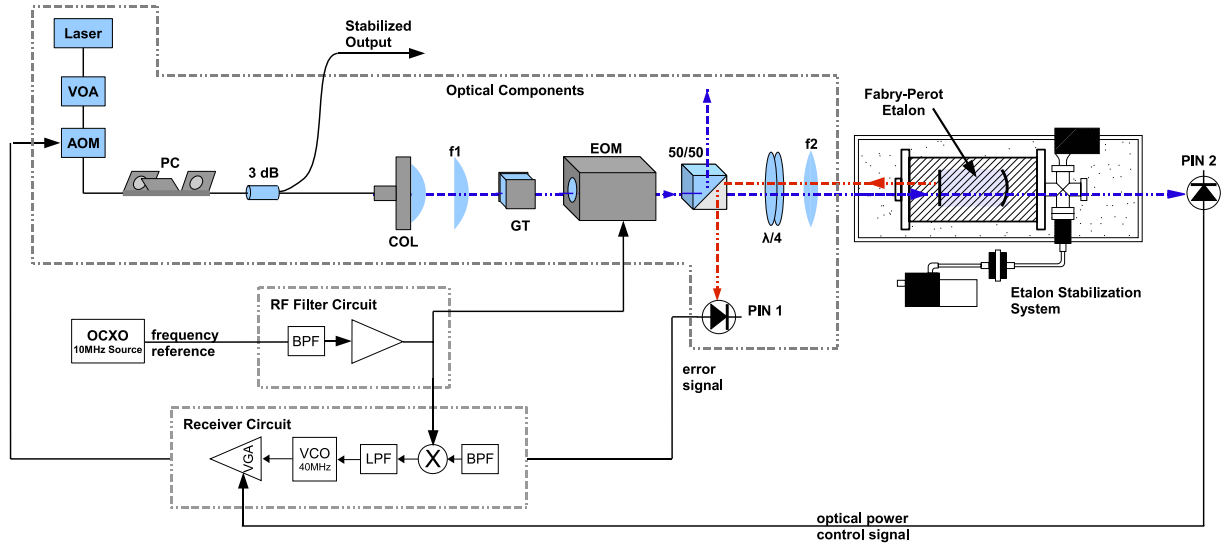
Fig. 3.1: Pound-Drever-Hall System Block Diagram

3.1   The Fabry-Perot Etalon

At the heart of the PDH system is a high-finesse Fabry-Perot cavity, or etalon. The FP resonant cavity is essentially a pair of highly reflective mirrors mounted to a stable spacer. If a laser is normally incident on the etalon such that the spacing between the two mirrors is an integer multiple of the laser wavelength, the light will experience constructive interference as it bounces back and forth inside the cavity. Under these conditions, the light intensity builds inside the cavity to an equilibrium value, and a small portion of the signal escapes through each mirror.

The beam exiting the front of the cavity is 180° out of phase with the reflected beam, canceling the reflection. The power exiting the rear of the etalon is equal to the incident power, and therefore the cavity appears transparent (Figure 3.2). Alternatively, if the laser is not at a resonant wavelength, the phase cancellation will not occur, and the incoming light will be almost completely reflected [12]. Note that the reflection spectrum is the inverse of the transmission spectrum in Figure 3.2.
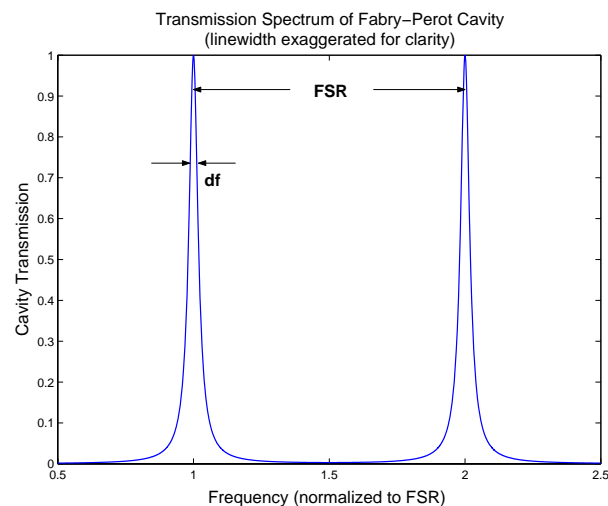
Fig. 3.2: Fabry-Perot Cavity Transmission Spectrum

The spacing between the resonant frequencies of the FP etalon is called the Free Spectral Range FSR, and it is a function of cavity length L and laser phase velocity. In the case of a free space cavity, the phase velocity is c, the speed of light.

$$FSR = \frac{c}{2L} \tag{3.1}$$

The reflectivity $\mathcal{R}$ of the etalon mirrors determines the intensity of light that eventually builds up in the cavity. A large value of $\mathcal{R}$ (over 0.999) will cause the average photon to bounce between the two mirrors many times before exiting the cavity. Under these conditions, the etalon is said to have a very high finesse $\mathcal{F}$. The larger the finesse, the more sensitive the etalon to small perturbations in the incident laser frequency. Therefore high-finesse FP cavities have very narrow transmission spectra and are said to have narrow Gaussian linewidth $\Delta\nu$.

$$\Delta\nu = \frac{FSR}{\mathcal{F}} \quad \text{, where} \quad \mathcal{F} = \frac{\pi\sqrt{\mathcal{R}}}{1-\mathcal{R}} \tag{3.2}$$

From these basic properties of the Fabry-Perot etalon, it is possible to generate an equation for the electric field reflection coefficient $F(\omega)$ as a function of the difference in the frequencies of the incident laser ω and the cavity resonance ω_0 [13]. Figure 3.3 shows a plot of this equation.

$$F(\omega_e) = \frac{E_{ref}}{E_{inc}} = \frac{\mathcal{R}\left[\exp\left(i\frac{\omega_e}{FSR}\right) - 1\right]}{1 - \mathcal{R}^2\exp\left(i\frac{\omega_e}{FSR}\right)} \quad \text{, where} \quad \omega_e \equiv \omega - \omega_0 \tag{3.3}$$

It is apparent from Figure 3.3 that the reflected optical intensity is symmetric about the cavity resonance frequency. If the feedback loop is designed such that the error signal is proportional to the reflected intensity, the system will never be able to determine which
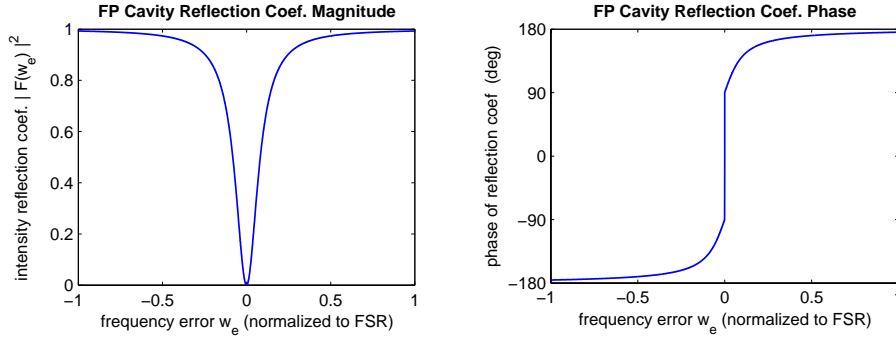
Fig. 3.3: Fabry-Perot Cavity Reflection Coefficient, Magnitude & Phase

side of resonance the laser is on. A stable, effective feedback loop must rely on the phase of the reflected light to determine the required adjustments to the input laser frequency.

3.2   The Pound-Drever-Hall Technique

The PDH technique[1] is a novel method of using the phase information of the reflected light to generate an accurate frequency error signal. It relies on an Electro-Optic Modulator (EOM) to phase modulate the incoming light before it is reflected by the etalon [1]. The modulation depth β is set such that the majority of the power is in the carrier and first order sidebands. Under these conditions, the electric field incident on the FP cavity can be very closely approximated by Equation 3.4 [13].

$$E_{inc} = E_0 e^{i(\omega t + \beta \sin \Omega t)} \approx E_0 \left[J_0(\beta)e^{i\omega t} + J_1(\beta)e^{i(\omega+\Omega)t} - J_1(\beta)e^{i(\omega-\Omega)t} \right] \tag{3.4}$$

The modulation frequency Ω is a single tone in the RF frequency range. This high-frequency modulation is required to push the sidebands far enough from the center frequency that they are totally reflected by the etalon when the center frequency is on resonance. In

---

[1] The derivation in this section and the next closely follows the development in Black [13].

other words, when $F(\omega_e) \approx 0$, $F(\omega_e \pm \Omega)$ is relatively large.

$$E_{ref} = E_0 \left[F(\omega_e) J_0(\beta) e^{i\omega t} + F(\omega_e + \Omega) J_1(\beta) e^{i(\omega+\Omega)t} - F(\omega_e - \Omega) J_1(\beta) e^{i(\omega-\Omega)t} \right] \quad (3.5)$$

The photodiode responsible for measuring the error signal (PIN 1 in Figure 3.1) measures the intensity of the field reflected by the etalon. Because $I_{ref} = |E_{ref}|^2$, the photodiode acts as a mixer. The three terms in Equation 3.5 beat with each other to produce tones at DC, Ω, and 2Ω. The beat signal with frequency Ω is generated by the mixing between the carrier frequency and each of the two sidebands. This is the useful portion of the beat signal, and bandpass filtering around Ω generates frequency error signal $I_e(t)$.

$$I_e(t) = 2 J_0(\beta) J_1(\beta) \Big\{ Re \Big[F(\omega_e) F^*(\omega_e + \Omega) - F^*(\omega_e) F(\omega_e - \Omega) \Big] \cos \Omega t$$
$$+ Im \Big[F(\omega_e) F^*(\omega_e + \Omega) - F^*(\omega_e) F(\omega_e - \Omega) \Big] \sin \Omega t + ... \ 2\Omega \ terms \Big\} \quad (3.6)$$

Recall that the modulation frequency Ω is large enough so that the sidebands of the incoming light are completely reflected. Figure 3.3 shows that the phase of the reflection coefficient approaches $\pm 180^o$ far from resonance. Therefore, at large Ω, $F(\omega_e \pm \Omega) \approx -1$, and Equation 3.6 can be simplified.

$$Re \Big[F(\omega_e) F^*(\omega_e + \Omega) - F^*(\omega_e) F(\omega_e - \Omega) \Big] \approx Re \Big[-F(\omega_e) + F^*(\omega_e) \Big]$$
$$= Re \Big[-2 Im \{ F(\omega_e) \} \Big]$$
$$= 0$$

$$I_e(t) = -2 J_0(\beta) J_1(\beta) Im \Big[F(\omega_e) F^*(\omega_e + \Omega) - F^*(\omega_e) F(\omega_e - \Omega) \Big] \sin \Omega t \quad (3.7)$$

Generated using equations 3.3 and 3.7, Figure 3.4 illustrates the dependence of the error

signal amplitude I_e on frequency error ω_e. Note that $I_e(\omega_e)$ has odd symmetry. The feedback system can now determine the exact laser frequency error because the PDH modulation scheme successfully extracts the phase information from the reflected light. Under feedback, the system is designed to operate in the steep linear region at the center of the graph below ($\omega_e \approx 0$).
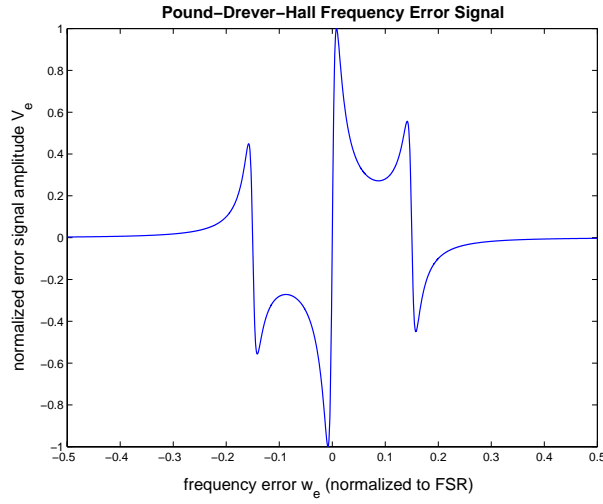
Fig. 3.4: Pound-Drever-Hall Normalized Error Signal

3.3   System Performance and Parameters

3.3.1   Sensitivity and Dynamic Range

The extremely high reflectivity of the FP etalon mirrors makes it possible to develop an approximate formula for the system sensitivity near resonance (when the laser is locked). Given that $R \approx 1$, the formula for finesse (Equation 3.2) can be easily approximated.

$$\mathcal{F} \approx \frac{\pi}{1 - \mathcal{R}^2} \tag{3.8}$$

Because the input laser is assumed to be locked, only small frequency perturbations are considered. Under this condition, Equation 3.3 can be expanded in a Taylor series about $\omega_e = 0$. Only the first two terms in the series are kept because (ω_e/FSR) is very small.

$$F(\omega_e) \approx \frac{\mathcal{R}\left[\left(1 + i\frac{\omega_e}{FSR}\right) - 1\right]}{1 - \mathcal{R}^2\left(1 + i\frac{\omega_e}{FSR}\right)} \tag{3.9}$$

Substituting 3.8 into 3.9 yields the approximate formula for the reflection coefficient under small frequency deviations $F(\delta\omega)$.

$$F(\delta\omega) \approx i\frac{\mathcal{F}}{\pi FSR}\delta\omega \tag{3.10}$$

Plugging the simplified expression for $F(\delta\omega)$ into 3.7 and assuming that $F(\delta\omega \pm \Omega) \to -1$, we obtain an approximation for the error signal when the laser is locked.

$$I_e(\delta\omega) \approx \frac{4J_0(\beta)J_1(\beta)\mathcal{F}}{\pi FSR}\delta\omega \tag{3.11}$$

The PDH system sensitivity M_{PDH} is defined below and estimated using Equation 3.11 and the FP cavity specifications in Table 4.1. The small frequency error $\delta\omega$ has been converted from rad/s to Hz (δf) for clarity. The total intensity incident on the etalon is assumed to be $I_{inc} = 200~\mu W$. The phase modulation depth has been chosen as $\beta = 1.08$, and the reason for this is discussed in detail in section 3.32.

$$M_{PDH} \equiv \frac{\delta I_e}{\delta f} = \frac{8J_0(\beta)J_1(\beta)\mathcal{F}}{FSR} \qquad \rightarrow \qquad \mathbf{M_{PDH} \approx 225\frac{nW}{Hz}} \tag{3.12}$$

Recall that the conceptual graph of error signal (Figure 3.4) contained a steep linear region near resonance. The slope of this curve is defined as M_{PDH}, and the linear range of

the curve defines the system's linear dynamic range Δ_{PDH}. Figure 3.5 shows the error signal curve specific to our FP etalon. From the graph, the linear dynamic range is graphically estimated to be $\mathbf{\Delta_{PDH}} = \pm \mathbf{15kHz}$. This figure was used during the optical alignment process (Section 7.2) to verify that the system has realized the full cavity finesse.
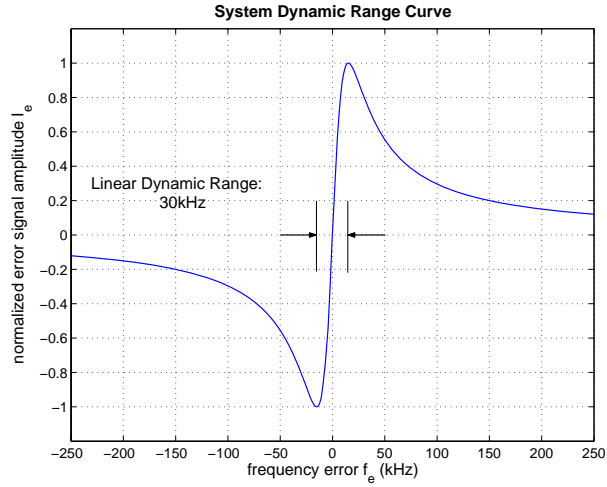
Fig. 3.5: Dynamic Range Calculation: Actual Error Signal Curve

3.3.2   Optimum Modulation Depth

It is evident from Equation 3.11 that the value of the modulation β can have a significant effect on the system sensitivity. By graphically choosing the value of β that produces the largest $[J_0(\beta)J_1(\beta)]$, the maximum value of M_{PDH} (shown in Equation 3.12) is realized. From Figure 3.6 it is clear that the optimum modulation depth to maximize system sensitivity is $\beta_{\mathbf{max}} = \mathbf{1.082}$. Calibration of β is achieved by adjusting the RF input power to the EOM.
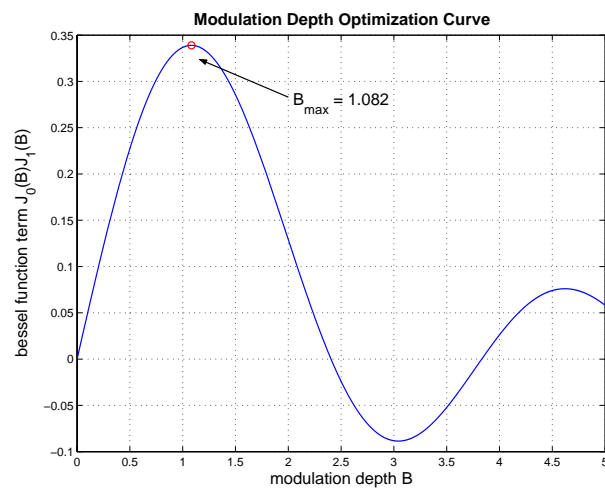
Fig. 3.6: Modulation Depth Optimization Curve

4. SYSTEM DESIGN: OPTICAL COMPONENTS

4.1 Input Laser

Although the PDH technique can theoretically be used to lock any input laser, the laser source in this system has a very narrow initial linewidth. The fiber laser from NP Photonics uses narrow-band Bragg gratings to define the lasing cavity, and achieves an estimated linewidth of 1-2 kHz [10]. Other Pound-Drever-Hall systems operating at shorter wavelengths are required to use dye, HeNe, or ND:YAG lasers [14], which have a much lower frequency stability than our fiber-based infrared laser. These systems implement a two stage locking process, in which a low-finesse FP cavity is used to "pre-lock" the laser before it enters the high-finesse frequency stabilization system [11].

The choice of infrared wavelength is what sets our system apart from other stabilized lasers. The longer wavelength allows the use of a more stable input laser, providing a better platform for stabilization. With the relatively high initial frequency stability in mind, the PDH system was designed using a simplified single-stage architecture (Figure 3.1). However, during the testing process, it was discovered that long-term frequency drift of the input laser exceeded the 30 kHz dynamic range of the PDH system (Section 7.2). In this case, a pre-locking stage is still required to maintain Continuous Wave (CW) stabilized output, but the advantages of a stable input laser are clearly seen in the short-term linewidth.

The laser wavelength can be thermally tuned, allowing coarse adjustments of the fre-

quency to bring it close to a resonant peak of the etalon. It produces a large 19 mW of output power, requiring the use of a Variable Optical Attenuator (VOA) at the input of the system. The VOA allows for coarse manual adjustments of the input power, and an electronic feedback loop makes fine adjustments in real time to control the optical intensity in the system. A 3 dB optical coupler splits the input laser into two signals: one for the Pound-Drever-Hall feedback system, and one to serve as the stabilized laser output.

4.2 Fabry-Perot Cavity Design

The Fabry-Perot etalon is in this system was designed by Dr. Jim Bergquist at NIST and manufactured to have the highest possible finesse. This extremely narrow-linewidth FP cavity is what gives the system the potential to achieve the maximum possible frequency stability. One of the etalon mirrors is planar and the other one is concave with radius $r_c = 50$ cm. Both have equal reflectivity. Table 4.1 illustrates the basic properties of this high-performance etalon.

Cavity Length	L	99.01	mm
Free Spectral Range	FSR	1.514	GHz
Reflectivity	$\mathcal{R}$	99.9995	%
Finesse	$\mathcal{F}$	628,000	
Linewidth	$\Delta\nu$	2.41	kHz

Tab. 4.1: Basic Fabry-Perot Etalon Specifications

The field inside the FP cavity can be modeled as a superposition of Hermite-Gaussian modes propagating back and forth between the two mirrors [15]. These Hermite-Gaussian modes are orthogonal solutions to Maxwell's equations under the assumption that the beam propagates along the z axis (Figure 4.1). Equation 4.1 describes the axial field distribution the fundamental Gaussian mode in the free space etalon. It is acceptable to consider only
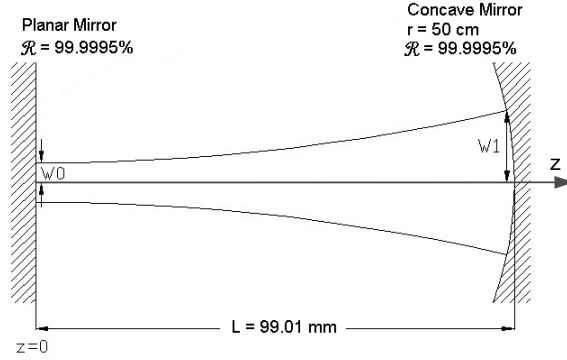
Fig. 4.1: Fabry-Perot Cavity Axial Modes

the fundamental transverse mode because a system of modematching lenses eliminates all other modes in the cavity.

$$E(\mathbf{r}, t) = E_0 \exp\left[i(\omega t - kz) - \frac{x^2 + y^2}{W^2(z)} - ik\frac{x^2 + y^2}{2R(z)} - i\phi(z)\right] \tag{4.1}$$

The Gaussian beam can be completely described by its beamwidth $W(z)$, the radius of curvature of its phase front $R(z)$, and its total phase $\phi(z)$. All of these terms are functions of the Rayleigh range z_0, which in turn is a function of the wavenumber k.

$$
\begin{aligned}
W(z) &= W_0\sqrt{1 + z^2/z_0^2} \\
R(z) &= z + z_0^2/z \\
\phi(z) &= \arctan\left(z/z_0\right) \\
z_0 &= kW_0^2/2
\end{aligned}
\tag{4.2}
$$

In order for a stable resonant field to exist inside the cavity, the radius of curvature of the wavefront must match the radius of curvature r of each mirror (Figure 4.1). In this way, the beam doubles back on itself as it is reflected, and the intensity builds inside the cavity.

The beamwidth on each mirror W_0, W_1 can be calculated by imposing this condition.

$$
\begin{aligned}
W_0 &= \frac{[4(Lr - L^2)]^{1/4}}{\sqrt{k}} = 0.3141mm \\
W_1 &= \sqrt{\frac{4L^2}{k^2W_0^2} + W_0^2} = 0.3512mm
\end{aligned}
\tag{4.3}
$$

4.3 Optical Modematching System

The most important component in shaping the beam profile as it propagates in free space is the input collimator, which controls the way the beam exits the optical fiber. Because the light exits a single-mode fiber with a highly-polished FC connector, the beam exiting the collimator can be assumed to be almost entirely composed of the fundamental Gaussian mode [16]. Any higher order Hermite-Gaussian modes in the Fabry-Perot etalon can only be excited by coupling from the fundamental mode due to beam misalignment [17].

Errors in the beam location and propagation angle were eliminated by proper positioning of the input collimator and other bulk optical components (Section 7.1). Even with the beam correctly centered on the axis of the etalon, inter-mode coupling can still be caused by any mismatch between the curvature of the beam phase front and the curvature of the cavity mirrors. The modematching system is designed to match the curvature of the beam to the Fabry-Perot etalon geometry, eliminating higher order modes in the etalon to produce the cleanest possible frequency error signal.

Because this system has only two degrees of freedom, it is sufficient to say that the incoming beam must be focused on the front mirror with a beamwidth of 0.3141mm. This condition is met by altering the incident beam with two lenses. Focal lengths f_1, f_2 and lens spacing distances $d_0 - d_3$ must be chosen to generate the correctly shaped beam incident on the FP cavity (Figure 4.2).
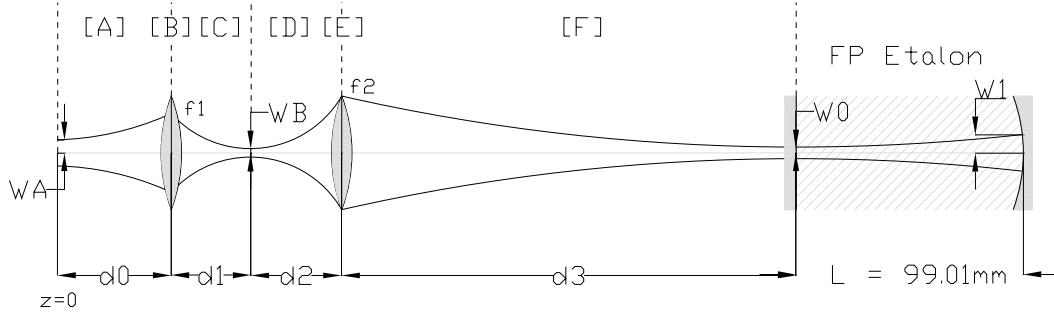
Fig. 4.2: Optical Modematching System

Propagation along the optical axis is described by the complex variable $q(z)$.

$$\frac{1}{q(z)} = \frac{1}{R(z)} - i\frac{2}{kW^2(z)} \tag{4.4}$$

Basic ray transfer matrices [15] can be used to describe each of the two lenses and four propagation regions in Figure 4.2.

$$
A = \begin{pmatrix} 1 & d_0 \\ 0 & 1 \end{pmatrix} \quad
B = \begin{pmatrix} 1 & 0 \\ -1/f_1 & 1 \end{pmatrix} \quad
C = \begin{pmatrix} 1 & d_1 \\ 0 & 1 \end{pmatrix}
$$

$$
D = \begin{pmatrix} 1 & d_2 \\ 0 & 1 \end{pmatrix} \quad
E = \begin{pmatrix} 1 & 0 \\ -1/f_2 & 1 \end{pmatrix} \quad
F = \begin{pmatrix} 1 & d_3 \\ 0 & 1 \end{pmatrix} \tag{4.5}
$$

Multiplying the individual matrices results in an equation for the Gaussian beam in the modematching system. The problem can be divided into two sections for clearer analysis: the region affected by lens 1 (represented by matrices A, B and C), and the region affected by lens 2 (represented by matrices D, E and F).

To develop an equation for Region 1, let the variable q_0 contain the properties of the beam at $z = 0$. The result, q_1 describes the focused beam between the two lenses, and is

determined by applying the ray transfer matrices to the Gaussian beam.

$$q_1 = \frac{a_1 q_0 + b_1}{c_1 q_0 + d_1} \quad , \text{ where } \quad \begin{pmatrix} a_1 & b_1 \\ c_1 & d_1 \end{pmatrix} = CBA \tag{4.6}$$

After some algebra, the resulting equation for Region 1 describes the focal distance d_1 and the waist of the focused beam W_B.

$$d_1 = \frac{4f_1 d_0^2 - 4f_1^2 d_0 + f_1 k^2 W_A^2}{4f_1^2 - 8f_1 d_0 + 4d_0^2 + k^2 W_A^4} \tag{4.7}$$

$$W_B = \sqrt{\frac{4}{k^2 W_A^4}\left(d_0 - \frac{d_0 d_1}{f_1} + d_1\right)^2 + W_A^4\left(1 + \frac{d_1}{f_1}\right)^2} \tag{4.8}$$

In Region 2, the same technique can be applied to produce very similar results. This time, the input variable is q_1, and the result, q_{FP} contains the properties of the beam as it strikes the planar mirror.

$$q_{FP} = \frac{a_2 q_1 + b_2}{c_2 q_1 + d_2} \quad , \text{ where } \quad \begin{pmatrix} a_2 & b_2 \\ c_2 & d_2 \end{pmatrix} = FED \tag{4.9}$$

$$d_3 = \frac{4f_2 d_2^2 - 4f_2^2 d_2 + f_2 k^2 W_B^2}{4f_2^2 - 8f_2 d_2 + 4d_2^2 + k^2 W_B^4} \tag{4.10}$$

$$W_0 = \sqrt{\frac{4}{k^2 W_B^4}\left(d_2 - \frac{d_2 d_3}{f_2} + d_3\right)^2 + W_B^4\left(1 + \frac{d_1}{f_1}\right)^2} \tag{4.11}$$

The incident beam properties are determined by the fiber collimator used in this system, which focuses the beam to an initial waist of $W_A = 1.05 \ mm$. Reasonable values for f_1 and f_2 are chosen, and the value of d_0 is set to be 15 mm, based on mounting constraints. Equations 4.7 and 4.10 can be used to determine focal distances d_1 and d_3 directly. The key

parameter in this system is the distance d_2, which is hidden more subtly in the equations above. Choosing the value of d_2 that yields the correct modematched beamwidth and focal point was found graphically using Matlab (Figure 4.3).
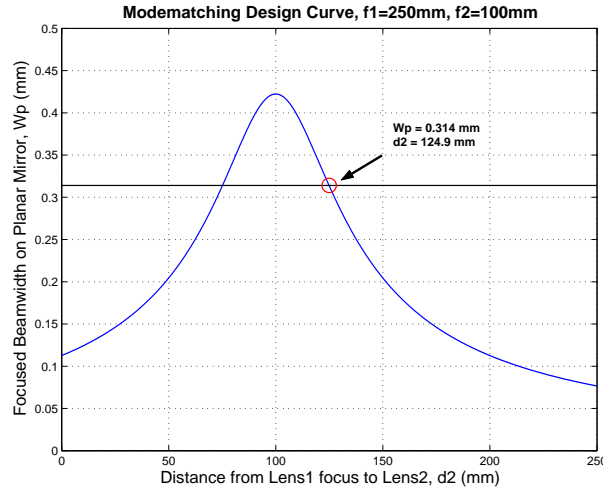
Fig. 4.3: Modematching System Design Curve

Although there are many possible combinations of f_1 and f_2 for modematching the system, the following geometry (Table 4.2) was chosen because it allowed enough room for the other optical components in the system. Lens 1 was chosen to be a plano-convex lens because of its close proximity to the input collimator, and Lens 2 was selected to be bi-convex. Both lenses are anti-reflection (AR) coated to minimize errors due to undesired reflections. Figure 4.4 illustrates the layout of the optical components and how they fit together with the modematching system.

f_1	250 mm	d_0	15 mm	W_A	1.05 mm
f_2	100 mm	d_1	247.8 mm	W_B	0.117 mm
		d_2	124.9 mm	W_0	0.314 mm
		d_3	279.7 mm	W_1	0.351 mm

Tab. 4.2: Modematching System Parameters
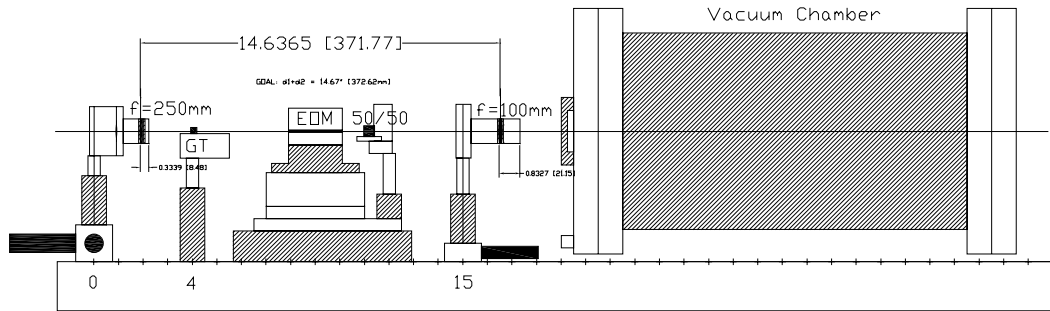
Fig. 4.4: Optical Component Layout

The system design produces very good results: the radius of the beam at the back mirror of the FP cavity is the correct 50 *cm*, and the average beamwidth is around 0.5 *mm* (Figure 4.5). This is a very tightly collimated beam, which passes cleanly through all the optical components, including the 2 *mm* aperture of the EOM.
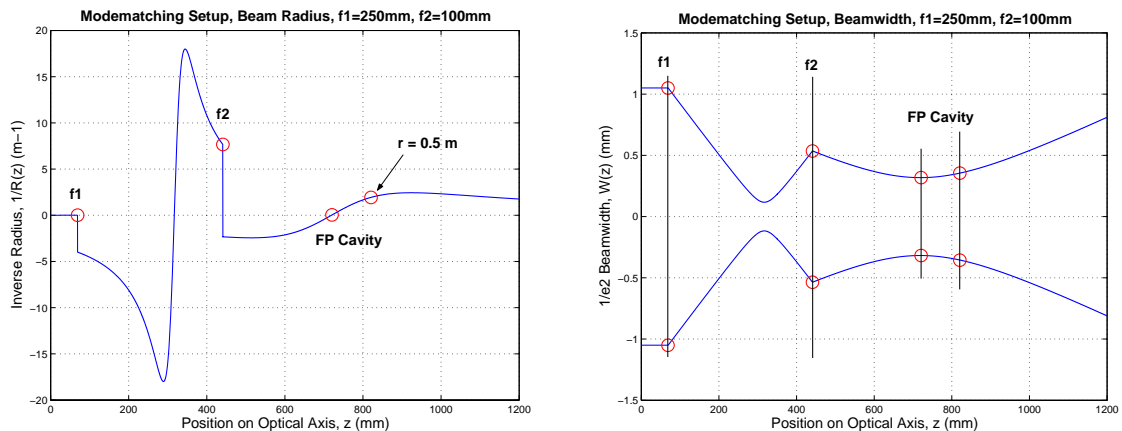
Fig. 4.5: Calculated Beamwidth and Radius

4.4   Polarization Control

To achieve the proper low-noise operation of the PDH system, the polarization of the incident light must be controlled at two critical locations: the input to the EOM and the input to the Fabry-Perot etalon (Figure 4.6). The MgO:$LiNbO_3$ crystal inside the EOM requires that

the incident light be vertically polarized. Polarization of the input beam is performed by a Glan-Taylor (GT) polarizing cube, which filters out the unwanted horizontal component. A simple fiber polarization controller is used to precondition the beam coming from the laser in order to minimize the amount of power lost at the Glan-Taylor cube.
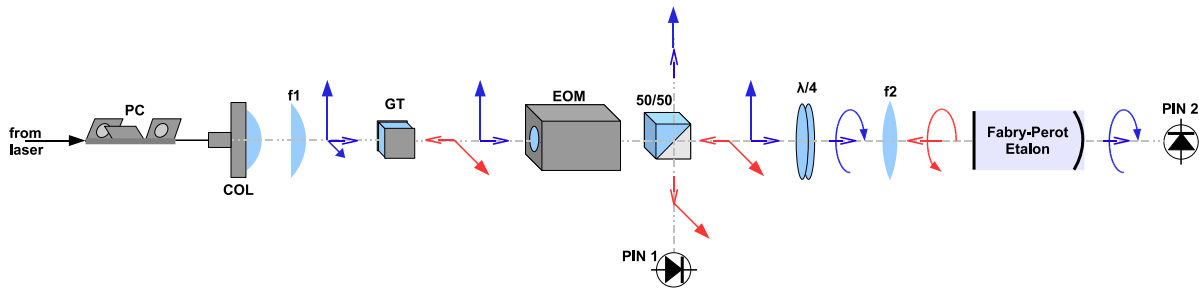
Fig. 4.6: Polarization Control System

The rationale behind the use of circular polarization in the etalon is more complicated. Even the highest quality Fabry-Perot mirrors exhibit some small level of birefringence due to stresses induced during fabrication of the mirror substrates and mounting to the etalon spacer. The result is that the light experiences a slightly different phase shift upon reflection (on the order of 0.1 μrad), depending on its state of polarization. In a high-finesse etalon, this minuscule effect multiplies to the point where there is a noticeable difference between the resonant frequencies of two orthogonal polarizations. Additionally, linearly polarized light can cause the mirror to develop a photorefractive "memory", which can lead to time-dependent birefringence noise. All of these effects can be avoided by using circularly polarized light, which rapidly averages the two birefringent states, and effectively erases the photorefractive memory as the polarization rotates [18].

A quarter-waveplate positioned in front of the etalon performs the conversion from vertical linear polarization to right-handed circular polarization. Upon reflection at the planar mirror, the polarization flips, and the reflected light is left-handed. As it passes

back through the quarter-waveplate, the backward-traveling beam is converted to horizontal linear polarization. Half of this light is directed toward the photodiode module PIN1 by a non-polarizing beamsplitter. The other half continues propagating toward the input, where it is completely rejected by the Glan-Taylor polarizer. In this way, the polarization control system also acts as an isolator, eliminating any reflected power that might destabilize the laser.

4.5   Frequency and Phase Modulators

There are essentially two feedback loops in the frequency locking system: one to reduce the laser frequency noise and one to reduce intensity noise. Through interaction between the beam and a 40 MHz acoustic wave, the Acousto-Optic Modulator (AOM) shifts the frequency of the incident light and diffracts the beam slightly. This diffraction provides an additional level of isolation of the reflected light. Generated by a VCO, the input to the AOM is a sine wave with a frequency centered on $f_c = 40\ MHz$ and proportional to the frequency error $\delta\omega$.

$$V_{RF}(t) = \sqrt{2P_{RF}}\sin\Big[(\omega_c - \delta\omega)t\Big] \tag{4.12}$$

The 3 dB bandwidth of the AOM is around 4 MHz, but by increasing the input power, a useful active range of about 6 MHz can be achieved. This wide bandwidth allows the user to manually "pull in" the laser frequency toward resonance from a relatively large initial offset value. Once initialized, the AOM has plenty of bandwidth to maintain the 30 kHz "lock-in range" defined by the high finesse of the FP etalon (Figure 3.5).

Small adjustments to the intensity of the light are made by adjusting the RF power supplied to the AOM, P_{RF}. For all acousto-optic devices, the relationship between insertion

loss and RF drive power is dependent on the wavelength, geometry, and material parameters. In this case, the AOM is designed to have a minimum insertion loss of $IL_0 < 2\ dB$ at $P_{RF} = 0.5\ W$. Derived from these parameters [19], Equation 4.13 shows the simplified AOM output intensity I_{AOM} as a function of input intensity I_0 and linear insertion loss η_0.

$$I_{AOM} \approx I_0 \eta_0 \sin^2 \left(\pi \sqrt{\frac{P_{RF}}{2}} \right) \quad , \text{where} \quad \eta_0 = 10^{-0.1(IL_0)} \tag{4.13}$$

The power control feedback loop is designed to operate in the range where the changes in I_{AOM} are most nearly linear. Figure 4.7 shows this range to be between $100 \leq P_{RF} \leq 400\ mW$, and the corresponding AOM loss ranges from $5.2 \leq IL(P_{RF}) \leq 2.2\ dB$.
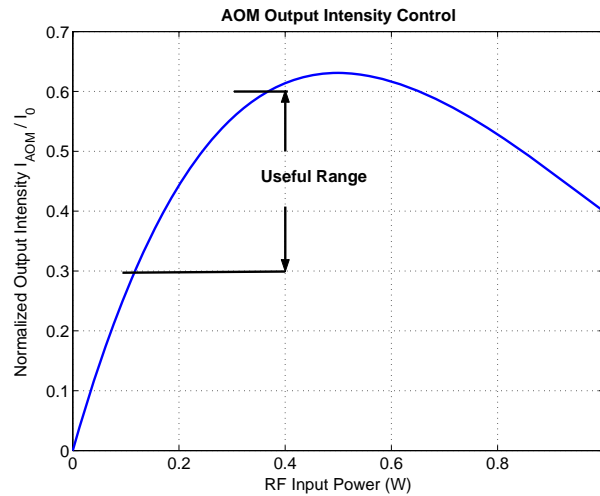
Fig. 4.7: AOM Intensity Control Curve

5. SYSTEM DESIGN: ELECTRONICS

The primary goal of the signal electronics is to implement the active feedback control of the laser frequency. This is accomplished by two separate analog circuits: one to filter and distribute the 10 MHz reference signal, and one to act as a receiver and signal conditioning circuit for the frequency error signal.

The RF filter circuit (Figure 5.1) is responsible for filtering the 10 MHz reference signal, amplifying it, and splitting it into high and low power outputs. The reference signal is generated by a low-noise Oven-Controlled Crystal Oscillator (OCXO) with frequency stability better than 0.1 Hz. Inside the filter circuit, a preamp matches the input impedance to 50 Ω, and cascaded high and low-pass filters remove the unwanted harmonics. The signal is then split, with one half going through a high-gain amplifier and providing as much as 1 W to the EOM. A buffer amplifier is required for this high-power output to keep the electronics from overheating. The low power output channel supplies the 10 MHz reference signal to the receiver circuit, where it is used to perform downconversion.
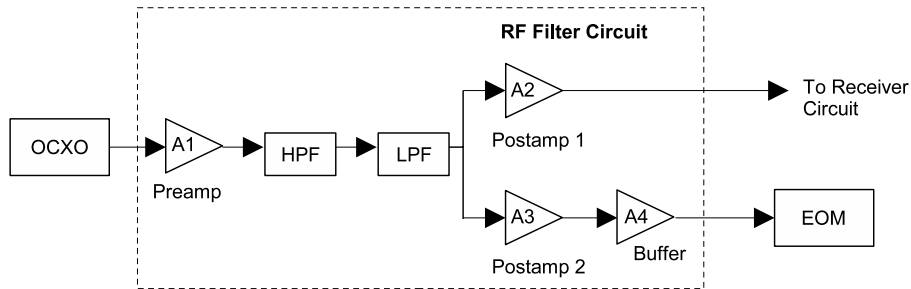
Fig. 5.1: RF Filter Circuit Block Diagram

Shown in Figure 5.2, the receiver circuit is designed to perform a wider range of tasks. At the front end, the circuit receives the frequency error signal from the amplified InGaAs photodiode module PIN1. This signal is first filtered through an inline 10 MHz bandpass filter to reduce noise. Also input to the receiver front end is the low-power RF reference signal direct from the RF filter circuit. Both these signals are passed through 50 Ω preamplifiers, and from there, the error signal is sent straight to the mixer. The RF reference signal passes through a three stage active phase delay circuit, which is adjusted to bring it into quadrature with the error signal. A double-balanced mixer downconverts the 10 MHz error signal to DC, and the low pass filter completes the process by filtering out the 20 MHz harmonic.

Fig. 5.2: Receiver Circuit Block Diagram

Now at baseband, the error signal is directly proportional to the frequency noise of the laser. A summing amplifier adds a constant DC offset, correcting the mean voltage so that the center frequency of the VCO is 40 MHz. The DC offset voltage is adjusted by tuning a potentiometer, and this process is performed to initialize the system and "pull in" the input laser frequency to match the FP etalon resonant frequency.

The receiver circuit also implements the optical power control loop. The large buildup of intensity inside the etalon heats the mirror coatings, which in turn changes the resonant

frequency on the order of 1 $Hz/\mu W$. This significant relationship has the potential to couple the intensity noise of the input laser into frequency noise in the final, stabilized output signal. Similar to the system used by Dr. Bergquist and the team at NIST [11], the amplitude control loop seeks to minimize this effect. A second identical photodiode, PIN2, mounted behind the etalon, measures the intensity of the light transmitted through the cavity. This signal is amplified and filtered by the receiver circuit. It is then sent to control a variable gain amplifier (VGA), which performs small adjustments of the 40 MHz RF output power P_{RF}. The final RF signal is sent to the AOM, where it directly controls the frequency and intensity of the incident light.

5.1   System Performance Simulations

The gain of amplifiers and frequency response of several key filters in the two circuits play a key role in determining the performance characteristics of the feedback loop. The RF filter circuit requires only one simple optimization: the level of the high-power output is set to produce the correct modulation depth of the EOM. In contrast, the optimization of the receiver circuit is much more complicated and requires detailed simulations. Using Matlab Simulink, the frequency control feedback loop and the intensity control loop were both simulated with the goal of choosing the optimum gain and frequency response characteristics inside the receiver.

5.1.1   Steady-State Optical Intensity Simulation

The primary goal the power control loop (Figure 5.3) is to keep the incident intensity on the Fabry-Perot etalon $Pinc$ in the range of 100 to 200 μW, while also generating a useful level of output power $Pout$ on the order of 1 mW. Simulation of this feedback loop takes

into account the measured insertion losses of all of the optical components in the system, including the GT polarizer, EOM, beamsplitter, and the vacuum chamber viewports. The input laser generates 12.8 dBm, and the VOA is used to make coarse adjustments to the input power level. Under feedback, the Variable Gain Amplifier (VGA) inside the receiver controls the RF power level P_{RF} to the AOM. The AOM, in turn, makes adjustments to the input optical intensity (Equation 4.13). The steady-state intensity setpoint is achieved by tuning the variable resistor R_{39}.
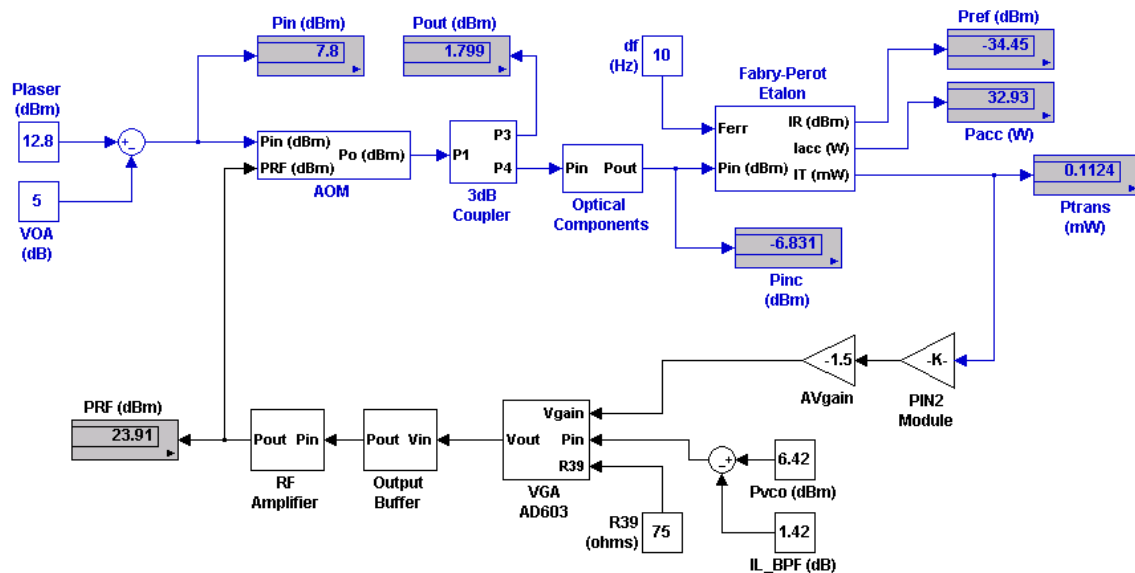
Fig. 5.3: Power Control Loop Simulation

Table 5.1 illustrates the simulated optical intensity levels at several important locations. It is important to note that the high finesse of the etalon causes almost 33 W of power to build up between the mirrors, which is why the incident power is set to a relatively low value.

P_{out}	Stabilized Laser Output	1.8	dBm
P_{inc}	FP Etalon Incident Power	-6.8	dBm
P_{trans}	FP Etalon Transmitted Power	-9.5	dBm
P_{acc}	FP Etalon Accumulated Power	33.1	W
P_{RF}	RF Power to AOM	0.25	W

Tab. 5.1: Simulated Optical Power Values

5.1.2   Frequency Noise Control Simulation

Modeling the operation of the frequency control loop begins with modeling the input laser as a frequency noise source. The narrow-linewidth fiber laser has a frequency noise power spectrum that is dominated by the flicker noise, or "pink noise", which has a $1/f$ frequency response [10]. Most lasers experience frequency noise with both pink and white components, but in this case, the manufacturer has pushed the white noise floor to a very low level. For the purposes of this analysis, the white noise contribution is ignored. Measured by NP Photonics, the frequency noise power spectral density $S_{\Delta\nu}$ of a similar laser is shown in Figure 5.4[1] and Equation 5.1.

$$S_{\Delta\nu}(f) \approx \frac{k}{f} \qquad (Hz^2/Hz) \quad \text{, where } k = 700^2 \quad Hz^3/Hz \tag{5.1}$$

Although it is prevalent in nature, pink noise is relatively difficult to simulate because a first order filter has a $1/f^2$ frequency response. Digital simulation of the input laser noise was performed using a modified[2] version of Voss's method [20], in which a series of white noise sources at different octaves are added to produce the pink noise signal.

Figure 5.5 shows the system model for the frequency control loop. The model is simplified by ignoring the math associated with the 10 MHz modulation and optical carrier.

---

[1] Figure 5.4 was reprinted with the permission of NP Photonics.

[2] The simulation method was modified by James McCartney, who improved Voss's method by delaying the noise sources so that they are out of sync. Details can be found at www.firstpr.com.au/dsp/pink-noise/
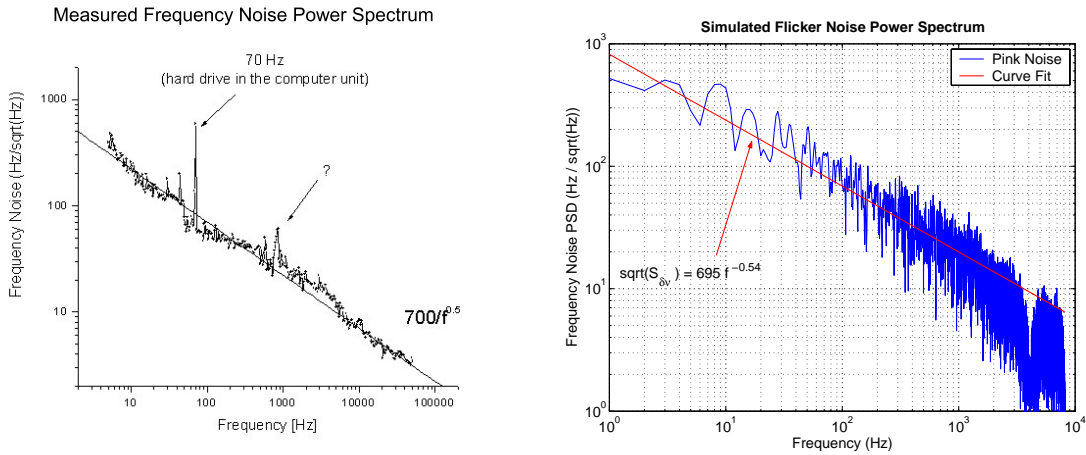
Fig. 5.4: Measured and Simulated Input Laser Frequency Noise PSD

The error signal is merely an idealized DC signal proportional to the frequency error in the linear range (Equation 3.11). The simulated flicker noise, in the time-domain, is used as the input to the model. All of the important amplifiers and filters inside the receiver circuit are modeled as separate elements for optimization. The block labeled "Frequency Comparator" is the simplified model for the Pound-Drever-Hall frequency measurement system, as defined by the equations developed in Chapter 3.
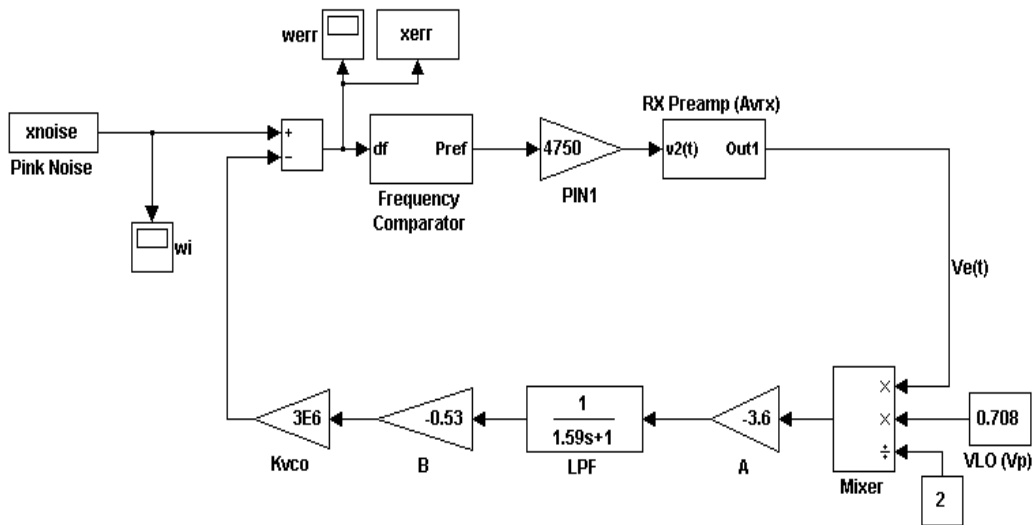
Fig. 5.5: Frequency Noise Control Loop Simulation

Through experimentation, an optimum combination of filter frequency response and amplifier gain was achieved. A single-pole lowpass filter with cutoff frequency of 0.1 Hz was used to produce the smallest possible frequency noise in the locked laser output. The resulting frequency noise PSD (Figure 5.6) has an unusual shape, due to the $1/f^2$ rolloff of the low pass filter. The system is essentially attempting to phase lock to a FM signal composed entirely of noise, and the filter response only matches the noise at low frequencies. This is evident in the output spectrum, which shows that the system achieves excellent noise cancellation below 1 kHz. At higher frequencies, the filter is too restrictive, and the system neglects to cancel a very small amount of high frequency noise.
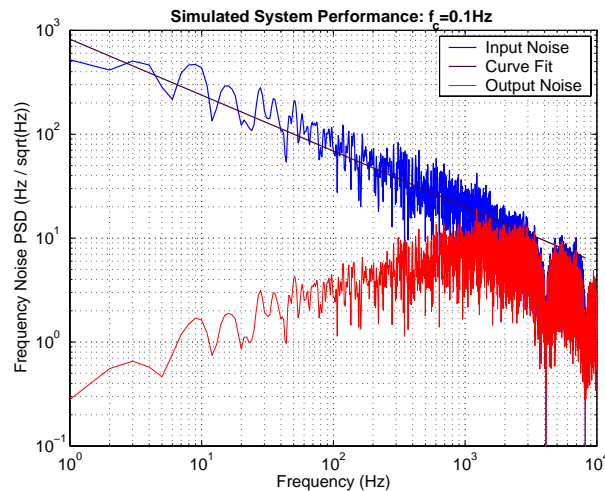
Fig. 5.6: Simulated Output Frequency Noise

5.2   Circuit Designs and Manufacturing

Both circuits were designed and built with the goal of low noise operation in mind. High quality active and passive components were chosen in the smallest practical surface-mount packages. Most of the active components in the circuits are of the SOIC package family, which is a small surface mount chip with 0.5 mm leads that can be soldered by hand. Both

circuits use a two-sided printed circuit board, the layout of which was carefully designed to minimize all of the RF signal path lengths. The use of small components allowed for a relatively high board density, but devices with the potential to create interference were placed farther apart, separated by a ground plane.

Manufacturing of the printed circuit boards was done by hand, using iron-on transfer paper. A mirrored, negative image of the circuit layout, printed onto the transfer paper, was applied to each side of the board, leaving a coating of ink. The boards were then etched in ferric chloride to remove the exposed copper. After populating the boards, each circuit was placed in its own inclosure to minimize external interference. Pictures of the finished circuits are shown in Appendix A.

5.3   Circuit Performance

Both the input filter and receiver circuits were independently tested to verify proper operation and noise performance. Noise figure and output SNR, output power, and harmonic rejection performance were verified for both circuits. A 500 MHz oscilloscope was used to sample and collect the data, and all processing was done via Matlab.

To calculate SNR, signals were sampled at 500 MHz for 500 μs. Because all of the signals in this system can be considered single-tone, a sinusoidal curve fit was applied to measure the noise. The rms error of the curve fit is equivalent to the rms noise, and therefore it was used in SNR calculations (Equation 5.2). This measurement technique accounts for all sources of noise, including amplitude and phase noise, and signal harmonics. All of these are referred to the form of amplitude noise in the calculation.

$$SNR = 20 \log \left(\frac{V_{RMS}}{RMSE} \right) \tag{5.2}$$

Harmonic rejection was measured by calculating the power spectrum in Matlab from the collected data. Welch's method [21] was used to calculate the one-sided PSD, from which the harmonics were measured. Figure 5.7 shows a small piece of the fitted data set used to calculate the SNR of the 10 MHz OCXO frequency reference, along with its power spectrum.
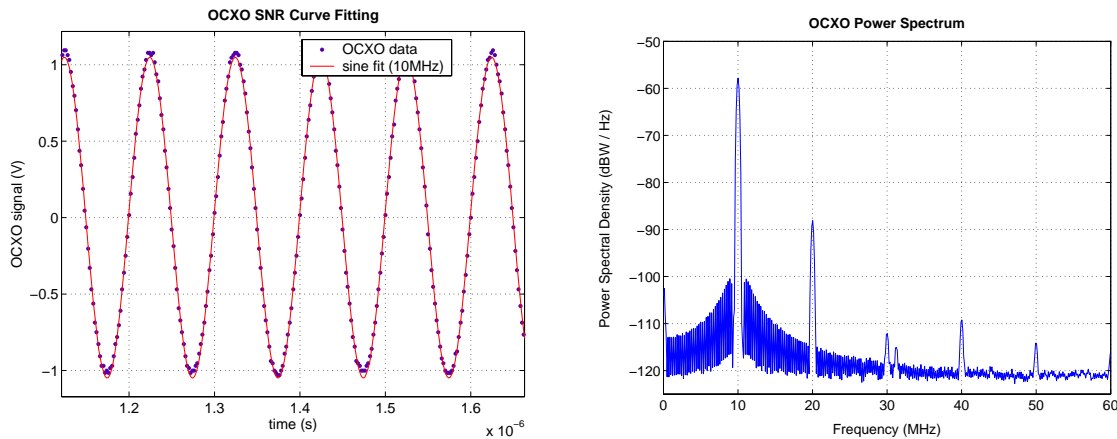
Fig. 5.7: RF Filter Performance Measurement

Table 5.2 shows the power, noise, and harmonic data for the RF filter circuit, which was calculated from measured data. Harmonic rejection by the low-power output is very good, while the high-power output does produce small, but noticeable harmonics. This is probably due to the output buffer amplifier, and the harmonic levels are still low enough to produce a clean signal for the EOM. Note that the noise figure for both output channels is negative because filtering reduces the total noise level.

Measuring the performance of the receiver circuit involved several steps. The output of the OCXO was split and sent to both the LO and RF input ports of the receiver. The phase delay circuit, which is capable of producing a shift of up to 210° in the LO signal, was adjusted to bring the two 10 MHz signals into quadrature. Signal quality measurements were then taken at the output of the mixer (V_{mix}), after the LPF (V_{dc}), and at the 40 MHz

	OCXO	LO Output	HI Output
Power (dBm)	10.4	7.8	24.0
1ST Harmonic (dBc)	-30.3	-53.2	-38.2
2ND Harmonic (dBc)	-54.2	-51.7	-42.2
3RD Harmonic (dBc)	-51.3	-59.0	-47.4
SNR (dB)	29.0	32.2	32.7
Noise Figure (dB)	–	-3.2	-3.7

Tab. 5.2: RF Filter Circuit Performance Data

RF output of the circuit (V_{out}).
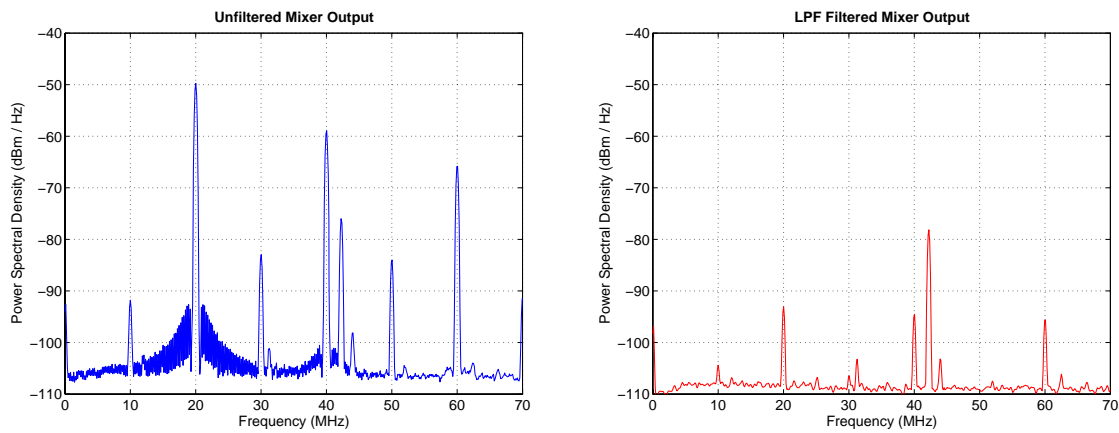
Fig. 5.8: Mixer Performance Measurement

The power spectrum of the downconverted signal, before and after filtering, is shown in Figure 5.8, and its harmonics are listed in Table 5.3. The low-pass filter does a very good job of reducing the higher order beat notes, and it leaves the DC component relatively unchanged. The spectral density of the peak measured at 42.2 MHz is also included in the table. It is the leakage from the VCO (V_{out}) detected by the measurement probe, and therefore it is not affected by the filter.

The output signal from the receiver circuit is produced by the 40 MHz VCO, but the output signal quality represents more than just the VCO noise performance. Because the VCO output frequency is determined by V_{dc}, output signal quality is also a measurement

Frequency	Mixer Output	LPF Output
f (MHz)	V_{mix} (dBm/Hz)	V_{dc} (dBm/Hz)
DC	-92.8	-97.0
10	-92.2	-104.6
20	-50.1	-93.6
30	-83.3	-106.6
40	-59.3	-94.9
42.2	-76.0	-78.5

Tab. 5.3: Mixer Power Spectrum Data
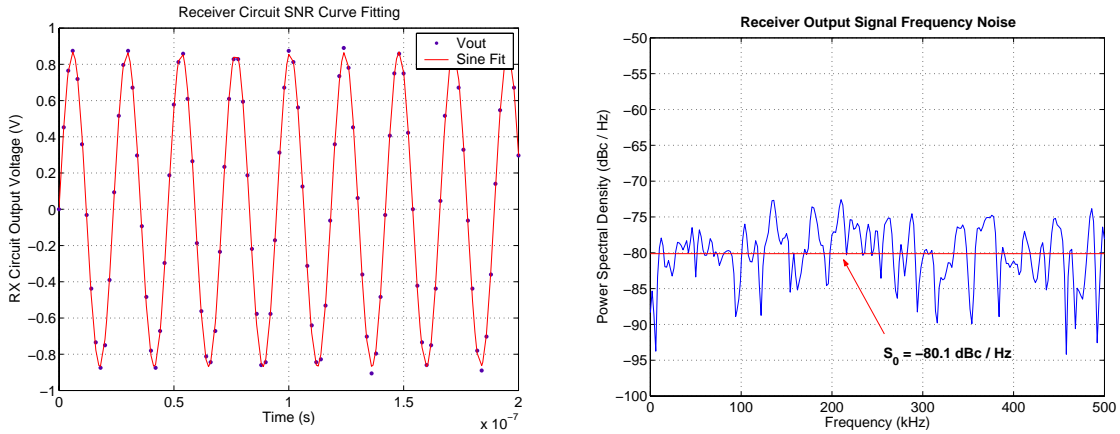
Fig. 5.9: Receiver Output Performance Measurement

of the stability of the entire receiver front end. In order to measure the short-term SNR of the signal and also its long-term frequency stability, the RF output signal was split into $N_{div} = 500$ sections, each with $\tau_{div} = 1 \ \mu s$ duration. The curve fitting method was used to measure the SNR of each data period (Figure 5.9), which was averaged to find the total SNR.

$$SNR = 20 \log \left(\frac{1}{\sqrt{2} N_{div}} \sum_{i=1}^{N_{div}} \frac{V_{rms}^{(i)}}{RSME^{(i)}} \right) = \mathbf{28.0 \ dB} \tag{5.3}$$

The frequencies of all the fitted curves were recorded and compiled to generate a picture of the total frequency stability of the receiver circuit. They represent a time-domain measurement of the receiver output frequency noise, with a sample rate of $f_{sdiv} = 1/\tau_{div} = 1 \ MHz$. The power spectrum of this frequency noise is shown in Figure 5.9. The power spec-

trum shows the frequency noise to be almost perfectly Gaussian, with a mean value of $-80\ dBc/Hz$. This is a reasonably low value, given that the system operates under constant feedback.

6. SYSTEM DESIGN: ENVIRONMENTAL STABILIZATION

The ultimate achievable frequency stability of the system is directly related to the finesse of the Fabry-Perot etalon (Equation 3.12). Based on the high reflectivity of the mirrors, the finesse of the cavity was calculated to be $\mathcal{F} = 628,000$, but this number is only valid if the mirrors are perfectly still. In order to achieve maximum possible stability, a comprehensive environmental stabilization system was developed to eliminate any mechanical and acoustic vibrations, pressure variations, and temperature fluctuations. By keeping the etalon in a temperature-controlled, mechanically isolated vacuum chamber, the frequency locking system can approach its theoretical resolution.

The critical parameter with regard to stabilization is the optical path length (OPL) of the Fabry-Perot etalon. Any minute change in the spacing between the two mirrors or the refractive index of the optical path causes a change in the phase shift of the beam in the cavity, and directly alters the resonant frequency. Equation 6.1 summarizes this relationship [14], where $\delta L_{OPL} = \delta(nL)$ represents minute changes in the optical path length, and $\delta \nu_{OPL}$ is the resulting change in cavity resonance (and also the stabilized laser frequency).

$$\delta \nu_{OPL} = \frac{2(FSR)\delta L_{OPL}}{\lambda} = \frac{2(FSR)}{\lambda}\Big(n\delta L + L\delta n\Big) \tag{6.1}$$

Equation 6.1 is used in the following sections to quantify the effects of environmental perturbations on the stabilized laser output, and to determine the requirements of these

stabilization systems.

6.1   Mechanical and Acoustic Isolation

Mechanical and acoustic vibrations are a major cause of line broadening in the Fabry-Perot cavity, and they are also the most difficult noise sources to eliminate. The designers of similar high-resolution frequency stabilization systems have all gone through great lengths to isolate mechanical noise in their systems [4, 11, 14, 22]. Our stabilized laser includes a low-cost vibration control system built to provide a reasonable level of mechanical stability (Figure 6.1). Future efforts to improve the quality of the frequency locking system will no doubt involve a more in-depth characterization of vibration, and a more complicated isolation system.
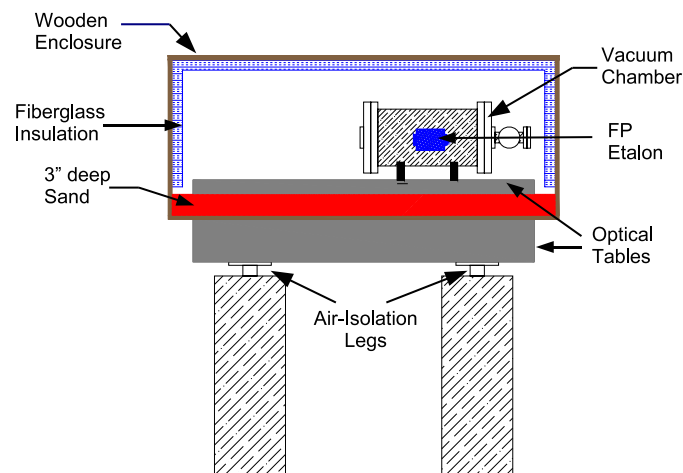
Fig. 6.1: Vibration and Acoustic Isolation System

Vibrations in the lab floor are primarily in the low frequency (below 50 Hz) range, and are therefore very difficult to eliminate. A two-stage system is employed to attenuate these vibrations as best as possible. Most of the isolation comes from a pressurized air floating

table system. The combined weight of the table and all components resting on the floating legs is estimated to be 700 *lbs*. Calculated from the manufacturers specifications for similar isolation legs [23], Figure 6.2 shows the estimated frequency response of the table.
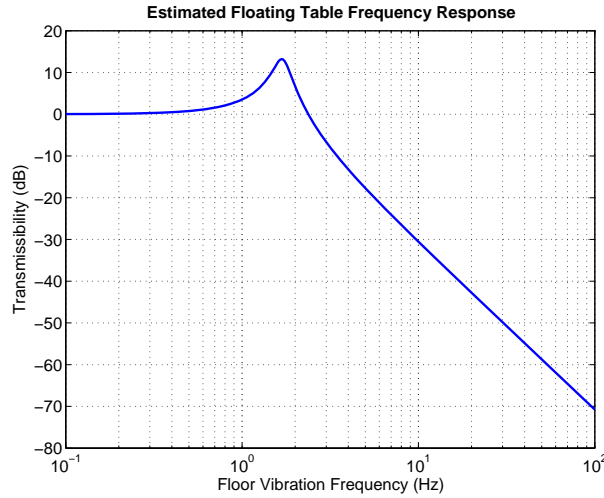
Fig. 6.2: Estimated Floating Table Vibration Isolation

The natural frequency of the floating table system is estimated to be 1.7 *Hz*. Above 3 *Hz*, the table provides good isolation, but in the low frequency range, particularly around system resonance, most of the floor vibration is efficiently coupled to the tabletop. The second stage of the vibration control system is designed to help with this low-frequency range. A second, smaller optical breadboard sits atop a large sandbox, 3" deep. Although it is difficult to analytically predict how well the friction between grains of dry sand effects the vibration isolation, the sandbox can be approximated as a viscous damper via the Kelvin-Voigt model [24]. This model describes the stress vs. strain (σ vs. ϵ) relationship in terms of the modulus of elasticity E and the viscosity η

$$\sigma(t) = E\epsilon(t) + \eta\frac{d\epsilon}{dt} \tag{6.2}$$

The frequency response of the sand $H(\omega)$ can be found by taking the Fourier transform

of Equation 6.2 and then calculating the ratio of strain over stress.

$$H(\omega) = \frac{\epsilon(\omega)}{\sigma(\omega)} = \frac{1}{E + i\omega\eta} \tag{6.3}$$

It is known that the viscosity η of dry sand is inversely proportional to the frequency of vibration ω such that the ratio $(\eta\omega/E)$ is constant [24]. This can be used to simplify the expression for the sandbox frequency response.

$$\frac{\eta\omega}{E} \equiv A_0 \quad \rightarrow \quad H(\omega) = \frac{1}{1 + iA_0} \tag{6.4}$$

Although the exact level of damping is unknown, Equation 6.4 illustrates that the sandbox damper has a relatively flat frequency response. At low frequencies, where the pneumatic table lacks good damping ability, the sandbox provides a needed boost in isolation.

Rudimentary acoustic isolation is provided by a large wooden enclosure with two doors for access to the optical components inside. The inside of the enclosure is lined with a 2" layer of fiberglass insulation, which provides about 6 dB of acoustic isolation [25]. This insulation also plays an important passive role in the temperature control system (Section 6.2). All testing and data acquisition was performed at night and in the early morning, when the vibration and acoustic noise levels in the lab were at a minimum.

6.2   Temperature Stabilization

Due to thermal expansion of the spacer between the two mirrors, even minute temperature fluctuations can have enormous effects on the resonant frequency of most Fabry-Perot cavities. This effect is often used to make highly accurate temperature sensors, but in this appli-

cation, any thermal expansion of the etalon spacer would be absolutely detrimental to the system performance. For this reason, the cavity spacer was constructed out of Corning premium grade ULE$^{\text{TM}}$(Ultra-Low Expansion) glass, which is approximately 93% SiO_2 and 7% TiO_2. This material has a very low coefficient of thermal expansion $|\alpha_{ULE}| \leq 30 \ ppb/^oC$ over a wide range of temperatures $(T = 5 - 35^oC)$.

Although α_{ULE} is quite low, it also changes with temperature, crossing from negative to positive at room temperature $T_{ULE} \approx 22^oC$ [26]. Figure 6.3 approximately illustrates this phenomenon[1]. Additionally, Corning has the ability to alter the concentration of titanium dopant in the glass, allowing them to create individual bools with custom T_{ULE} values. The ULE spacer in this system was manufactured to have $T_{ULE} \approx 30^oC$. This requires the temperature control system to maintain an elevated temperature in the vacuum chamber, causing it to be in constant feedback and thereby maximizing the accuracy of temperature control. The result is that at a temperature of 30^oC, the etalon spacer has a $\alpha_{ULE} \approx 0$, and small fluctuations in temperature have no effect on the cavity length.
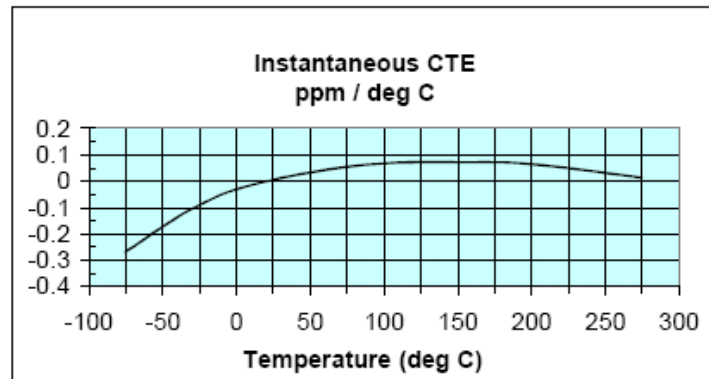

Fig. 6.3: Corning ULE$^{\text{TM}}$Glass Thermal Expansion Curve

The goal of the temperature control system is clearly to keep the temperature as stable as possible, at a mean value of 30^oC. This was achieved through a system of resistive wire

---

[1] This graphic was borrowed from the Corning ULE$^{\text{TM}}$datasheet with the permission of Corning, inc.

heating elements and a PID temperature controller. There is no real, exact data available for the temperature at which the zero-crossing ULE™glass occurs, possibly due to variations between individual bools. Therefore, it can be assumed that T_{ULE} is not exactly 30^oC, and the temperature setpoint must be adjusted experimentally until an optimal temperature value is reached. For this reason, a homemade PID controller was constructed using Matlab, a DAQ card, and some basic analog electronics. Because it has no set-point resolution limitation[2], this PID controller can be precisely tuned so that the FP cavity spacer has a CTE of exactly zero.

6.2.1   Temperature Measurement

Under vacuum, the FP cavity spacer exchanges thermal energy with the inside of the chamber walls via electromagnetic radiation. Over time, the system reaches equilibrium, and the amount of energy radiated by the glass spacer is equal to the amount of incident energy it absorbs. Under these conditions, it can be assumed that the temperature of the etalon is equal to the temperature of the chamber walls. Therefore, in a highly stable system, it is possible to indirectly probe the temperature of the etalon by measuring the temperature of the vacuum chamber wall.

This task is accomplished by a thermistor mounted to the top of the vacuum chamber, on the outside of the cylinder wall. Silicon grease is used to improve the thermal coupling between the chamber wall and the sensor element. Thermistors are an ideal choice for this application because of their high accuracy, which is limited only by the SNR of the measurement electronics. The drawback of a thermistor sensor is that it has limited absolute

---

[2] Most commercial PID controllers have a set-point resolution limit of about 0.1^oC. It is important to note that even though the user can only set the temperature in increments of 0.1^oC, most PID controllers have the ability to control temperature much more accurately, depending on the thermal mass and stability of the system under control.

accuracy due to nonlinearity and manufacturing variations. Fortunately, this is not a problem because the exact temperature set-point is unknown, and therefore information about the exact temperature is not a required quantity. Once T_{ULE} has been experimentally reached, the system must simply maintain that temperature.
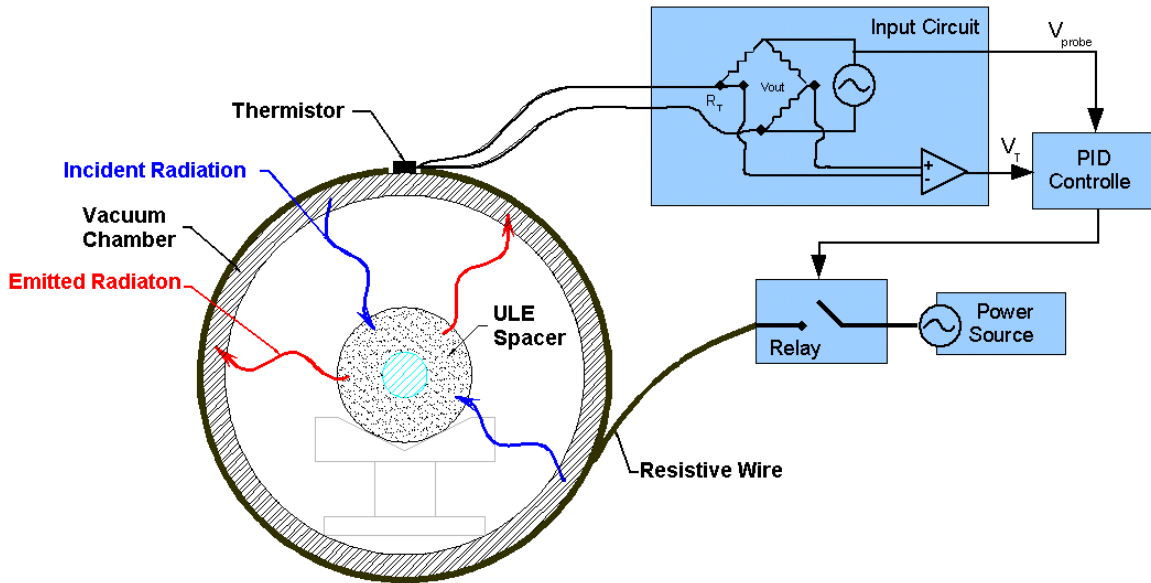
Fig. 6.4: Temperature Stabilization System

An amplitude-stabilized Wein-bridge oscillator provides the $600\,Hz$ probe signal $V_{probe}(t)$ for the thermistor. This signal is then interpreted by a simple wheatstone bridge circuit and a differential amplifier (Figure 6.5). A data acquisition card measures the single-ended output from the amplifier $V_T(T)$, along with $V_{probe}(t)$. The Matlab software grabs the data, performs a low-resolution FFT of each signal, and then picks out the $600 \pm 50Hz$ component. This method effectively measures the rms amplitude of each signal while filtering out most of the noise. The signal processing program then references V_T to the amplitude of the

probe source, so as to avoid any error due to amplitude fluctuations.

$$\Delta V(T) = \frac{V_T(T)}{V_{probe}} \tag{6.5}$$
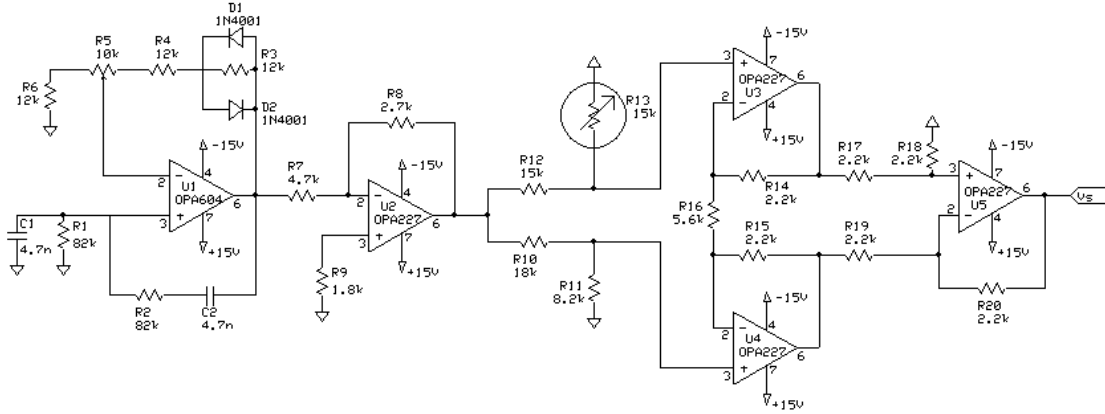
Fig. 6.5: Temperature Controller Input Circuit Schematic

A simple calibration of the thermistor was performed by mounting it, along with a type-K thermocouple, to the top of the vacuum chamber and running the whole chamber through a heating and cooling cycle. The thermocouple was connected to a digital temperature monitor with 1^oC resolution, so data points were taken at 1^oC intervals. Because of this limited resolution, the calibration data showed a significant amount of artificial hysteresis. The heating and cooling cycle temperature data (T_{heat}, T_{cool}) was modified to reflect the actual measured temperature, removing the hysteresis.

$$T_{actual} = T_{heat} - 0.5^oC = T_{cool} + 0.5^oC \tag{6.6}$$

Figure 6.6 shows good agreement between the adjusted heating and cooling data. These two curves were averaged and a quadratic curve fit was performed (Equation 6.7). Although the thermistor curve was expected to be exponential [27], in the local region from $23 - 43^oC$,

the quadratic fit produced the smallest rms error $E_{rms} = 0.08^oC$ of any curve fitting method. It is reasonable to assume that temperature measurements made using the thermistor are accurate to within about $\pm 0.1^oC$ of the true value.

$$T_{meas}(\Delta V) = 2.833\Delta V^2 - 22.99\Delta V + 39.99 \tag{6.7}$$
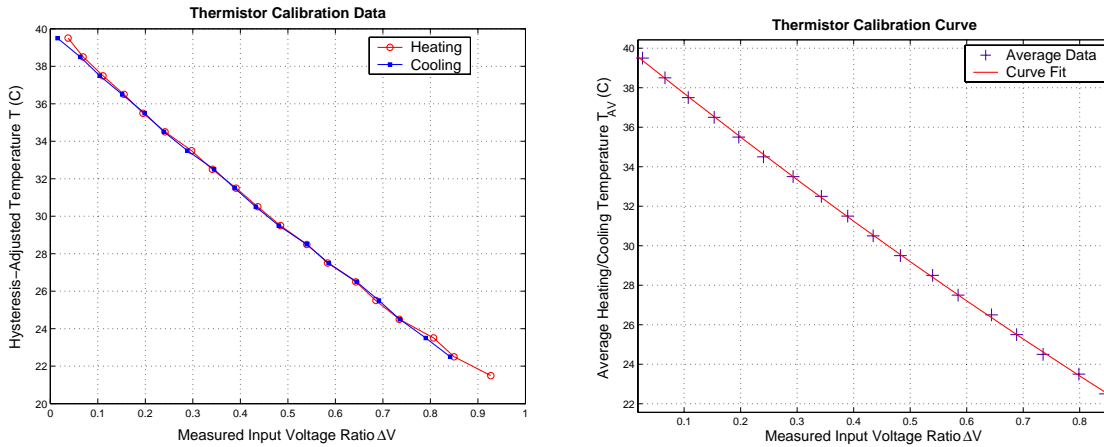
Fig. 6.6: Thermistor Calibration Curve

Although the accuracy of the thermistor is relatively low, the sensor's precision is extremely high. Figure 6.7 illustrates several minutes of temperature data taken by the thermistor system while the vacuum chamber was at a stable equilibrium. In this case, the doors to the acoustic enclosure had been closed overnight, and the chamber had stabilized to room temperature. Temperature readings were taken at one second intervals, and each reading was an average of 40 independent measurements. The data was fitted to a 9th order polynomial curve to extract the general trend.

Figure 6.7 shows that the rms error between the data points and the trend line is very small $\sigma_{40} = 0.0011^oC$. If each measurement is assumed to be independent, than the rms error for N averaged measurements is given by Equation 6.8. The precision for a single
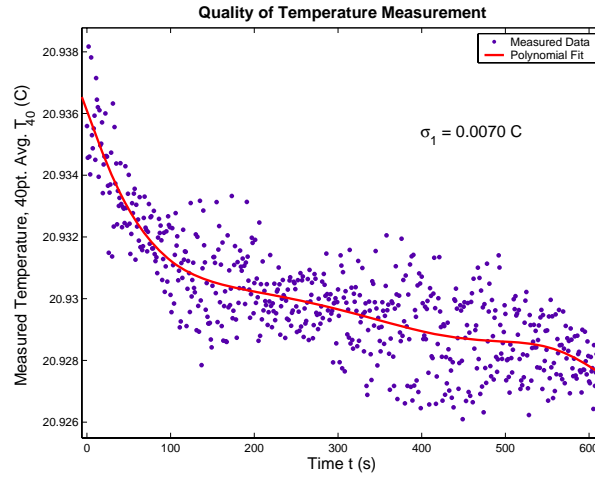
Fig. 6.7: Thermistor Precision Curve

measurement can be easily calculated as $\sigma_1 = \mathbf{0.0070^{o}C}$

$$\sigma_N = \frac{\sigma_1}{\sqrt{N}} \tag{6.8}$$

6.2.2   Temperature Controller

The temperature controller was written as Matlab software with a built in GUI to display a monitor graph of the system temperature and to allow the user to change the control parameters during operation. It reads temperature measurements using the FFT technique described above and uses a PID algorithm (Proportional, Integral, Derivative) to calculate the amount of power to supply to the heating wire.

The basic PID algorithm is shown in Equation 6.9 and can be used in almost any kind of control system with good results [28]. In this case, the algorithm is designed to maintain the temperature $T(t)$ at setpoint T_0 by generating a heater power $u(t)$.

$$u(t) = P\left[\left(T(t) - T_0\right) + I \int \left(T(t) - T_0\right)dt + D\frac{dT}{dt}\right] \tag{6.9}$$
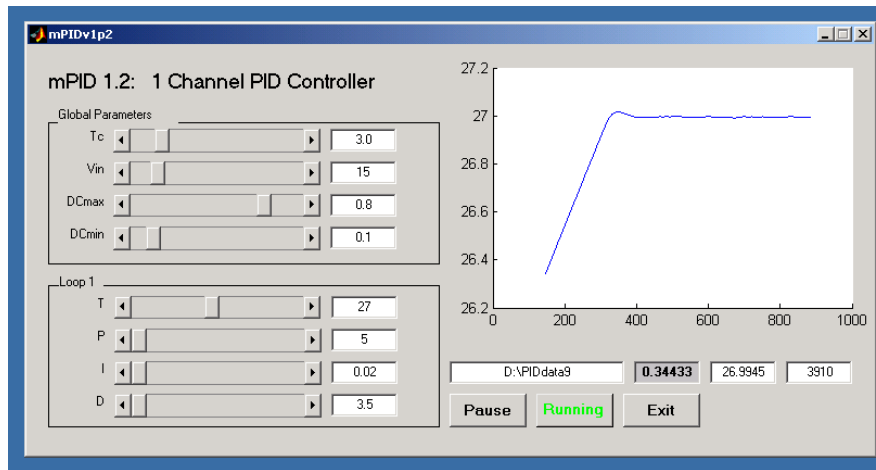
Fig. 6.8: PID Controller Screenshot

A master clock governs the controller's operation, and the cycle time can be set by the user in the range $1 \leq T_c \leq 100$ seconds. A time of $T_c = 3$ s was found to give the best results. Each clock cycle, the controller makes as many temperature measurements as possible, and then uses the PID algorithm to calculate the required power to send to the heater. The controller output is in the form of a square wave with a duty cycle proportional to the required power. The square wave output is sent to a solid state relay, which switches an AC source on and off, supplying the actual power signal to the resistive wire coil.

6.2.3   Temperature Controller Tuning and Performance

To optimize the performance of the temperature controller, the PID constants were tuned using Astrom's method [28]. This technique involves turning the controller on in "P mode" $(D = I = 0)$, and increasing P until the system just begins to oscillate. The period of oscillation and value of P are recorded and used to set the PID constants to match the dynamic properties of the system. In this case, the optimum performance was realized when the control loop had a total phase margin of 60°, which occurred when the PID constants had

the following values. Note that the damping constant D is very large because the vacuum chamber has a huge thermal mass and takes a very long time to react to stimuli from the controller.

P	19.0
I	0.016
D	14.70

Tab. 6.1: PID Constants

By keeping the temperature controller running during the assembly and alignment process, a huge amount of performance data was generated. Figure 6.9 shows the performance of the controller as it brings the system up from room temperature to 30^oC. A detail of the steady-state performance is also shown. Figure 6.9 also illustrates the importance of the acoustic enclosure, which provides an additional level of passive temperature control, isolating the entire system from external thermal perturbations. With the doors of the enclosure closed, the system temperature is 5 times more stable than with the doors open (Table 6.2).

	Mean Temp. T_0 (^oC)	Standard Deviation σ_T (^oC)
Door Open:	30.000	0.011
Door Closed:	30.000	0.002

Tab. 6.2: Temperature Controller Performance Data

Test data shows that the PID controller can maintain a constant temperature of 30^oC, with a 2σ tolerance of $\pm 0.004 \, ^oC$ on the outer wall of the vacuum chamber. It was previously assumed that under long-term equilibrium conditions, the temperature of the FP cavity spacer was equal T_{FP} to the temperature of the chamber wall T_{wall}. It is important to quantify how the small, short term oscillations in T_{wall} affect T_{FP}. Because there is no way of directly monitoring the temperature of the FP cavity, these effects must be calculated
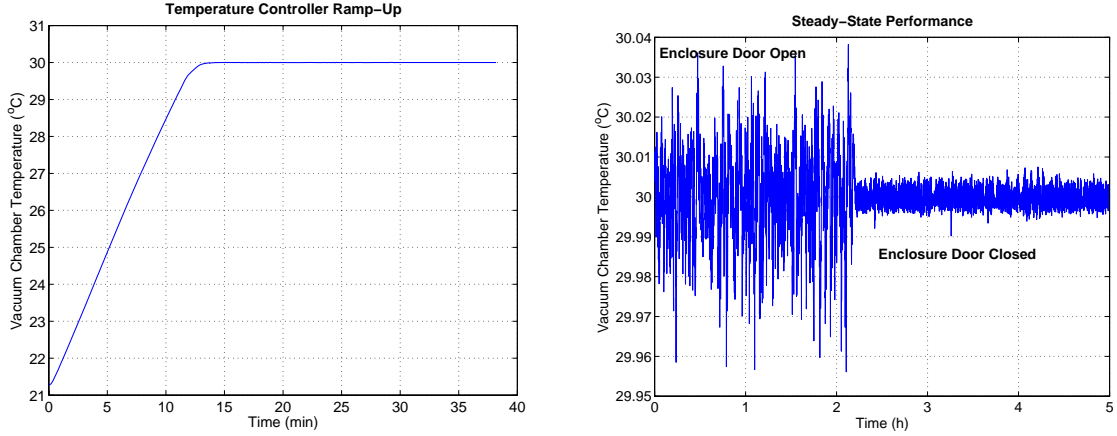
Fig. 6.9: Temperature Controller Performance Curves

analytically.

If the chamber is under a good quality vacuum, then the heat transfer between the FP cavity and the chamber walls is predominantly through electromagnetic radiation. Several groups have estimated the time constant of this coupling to be on the order of $\tau = 24$ hours [4, 22]. Although radiative heat transfer varies with T^4, the time constant estimation implies that under very small fluctuations in a highly damped system, the process can be approximated by the linear first order differential equation that governs conduction [29]. In this case, $\delta T_i = T_i - 30^oC$ represents the temperature deviation from the setpoint.

$$\frac{d}{dt}\delta T_{FP} \approx \frac{1}{\tau}\left(\delta T_{wall} - \delta T_{FP}\right) \qquad \Rightarrow \qquad \delta T_{FP} \approx \delta T_{wall}\left(1 + e^{-1/\tau}\right) \tag{6.10}$$

From Equation 6.10, the standard deviation of the etalon temperature $\sigma_{T(FP)}$ can be estimated.

$$\sigma_{T(FP)} \approx \sigma_{wall}\left(1 + e^{-1/\tau}\right) = 2.3x10^{-8} \ ^oC \tag{6.11}$$

The linewidth broadening due to temperature fluctuations, $\sigma\nu_T$, can be estimated by applying Equation 6.1. Even at the maximum value of α_{ULE}, the temperature control

system is still capable of providing a very high level of linewidth stability. However, as T_{FP} approaches T_{ULE}, the line broadening due to temperature fluctuations is approaches zero. This shows the importance of maintaining the correct temperature in the vacuum chamber.

$$\sigma\nu_T = \frac{2FSR}{\lambda}\Big(nL\alpha_{ULE}\sigma_{T(FP)}\Big) \leq \textbf{0.135 Hz} \tag{6.12}$$

6.3   Vacuum System

The vacuum system is designed to stabilize of the refractive index part of the OPL ($L_{OPL} = nL$). The glass spacer between the mirrors has a hollow core and a ventilation tube so that the region where the the beam propagates can be evacuated (Figure 6.10). The entire etalon is placed in a vacuum chamber capable of maintaining an extremely high vacuum for long periods of time. A high-vacuum rotary vane pump is used to reduce the absolute pressure to $P \approx 0.01 \, torr$, and a filter element keeps the vaporized pump oil from entering the chamber. The pump inlet line is equipped with two valves, one to seal off the vacuum chamber and one to seal off the oil trap so that it does not absorb moisture from the atmosphere. During system operation, these valves are sealed and the pump remains off to reduce mechanical noise.

Flat high-vacuum viewports are mounted on the optical axis, one on each end of the cylindrical chamber to allow for beam propagation. These windows are anti-reflection coated to minimize error. Measured with a simple Bourdon tube gauge, the system showed no perceptible leakage over a period of one month.

If the small amount of air left inside the chamber is considered an ideal gas, then the pressure and temperature fluctuations are related by the ideal gas law. The vacuum chamber has an approximate volume of $V = 11.53x10^{-3} \, m^3$, the mean temperature is $T = 30^oC$, and
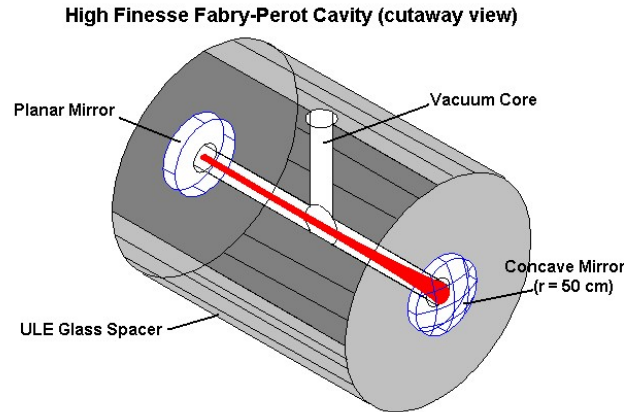
Fig. 6.10: FP Etalon Vacuum Core

the pressure is $P \approx 0.01\ torr$. The number of moles of gas left in the chamber is represented by n_g.

$$n_g = \frac{PV}{RT} = 6.10x10^{-6}\ moles \tag{6.13}$$

In the sealed chamber, any changes in pressure are brought about by changes in temperature, so the vacuum system can be considered as an extension of the temperature stabilization system. The ideal gas law is used a second time, along with the molar quantity of gas in the chamber, to calculate the effect of temperature changes on pressure.

$$\frac{dP}{dT} = \frac{n_g R}{T} = 4.4x10^{-3}\ Pa/^oC \tag{6.14}$$

The stability of the refractive index inside the etalon is given by σ_n, and it can be calculated using the chain rule. The value of σ_n is extremely small because the temperature of the etalon is quite stable and the rate of change of refractive index with respect to pressure

is very small: $dn/dP \approx 3x10^{-9} \ Pa^{-1}$ [22].

$$\sigma_n = \frac{dn}{dP}\frac{dP}{dT}\sigma_{T(FP)} = 3.03x10^{-19} \tag{6.15}$$

Equation 6.1 can be used to calculate the effects of these refractive index fluctuations on the etalon linewidth, $\sigma\nu_n$. The results of Equation 6.16 show that, given the high level of temperature control, the modest vacuum level of 0.01 torr is sufficient to eliminate pressure fluctuations in the optical path as a source of line broadening.

$$\sigma\nu_n = \frac{2(FSR)}{\lambda}\Big(L\sigma_n\Big) = \mathbf{6x10^{-5} \ Hz} \tag{6.16}$$

7. SYSTEM ASSEMBLY AND RESULTS

7.1 Assembly and Alignment

. Because this system involves a large number of very different subsystems and components, putting everything together proved to be a very challenging process. The most important and difficult task was aligning the bulk optical components that guide the beam as it propagates in free space. The position and angle of these components are what define the optical axis, state of polarization, and beam width and phase front radius throughout the system. The high finesse of the FP etalon makes it very sensitive to any errors in alignment or beam properties, and infrared wavelength adds an additional challenge to the alignment process.

Through experimentation, a step-by-step technique was developed to bring the various bulk optical components into alignment. Several laser sources were used at different stages of the process to measure different properties of the system. Enclosed by the vacuum chamber, the Fabry-Perot etalon defines the center of the system. The planar mirror of the cavity faces the incoming beam, and its axis was made as level as possible before closing the vacuum chamber. All other lenses, polarization and electro-optical devices are held by fully adjustable mounts, and their positions and orientations were adjusted to bring the beam into accordance with the stationary Fabry-Perot cavity.

7.1.1   Establishing the Optical Axis

The first step in the alignment process was to establish the optical axis, which is defined by the z-axis of the Fabry-Perot cavity. All optical components except the etalon and the input collimator were removed from the system. A 633 nm Helium-Neon (HeNe) laser was used for the coarse alignment of the collimator. The red visible light was sent through an attenuator and then coupled into the input fiber. The mirror coatings of the etalon were experimentally determined to be only partially reflective at 633 nm, so the reflected beam produced two spots, a large spot from the front mirror reflection, and a focused spot produced by the curved back mirror. The $(x - y)$ position and angle of the input collimator were adjusted to bring the two reflected spots together with the incoming beam.

Next, the visible light source was replaced with the narrowband laser centered on 1550 nm. A coupler and photodetector were set up to measure the reflected intensity coupled back into the input fiber (Figure 7.1). This level was extremely low due to the narrow core size of the single-mode fiber. Under normal system operation, this is a positive effect because it means that the input fiber adds an additional level of isolation. For alignment purposes, the loss of the VOA was reduced so that the input power to the coupler was 5 dBm, producing a detectable level of re-coupled reflected power. Because the mirror reflectivity is almost 100% at 1550 nm, this test only measures the beam reflected by the first mirror. Therefore, the re-coupling test was used to fine-tune the angle of the input collimator only, and the position was left alone.

With the input angle established, and the input collimator position nearly established, the 3 dB non-polarizing beamsplitter cube was added to the path. This cube was adjusted to maximize the reflected power received by the photodiode module PIN1. Fine adjustment of the collimator position was performed using a 1310 nm laser diode source, which experiences
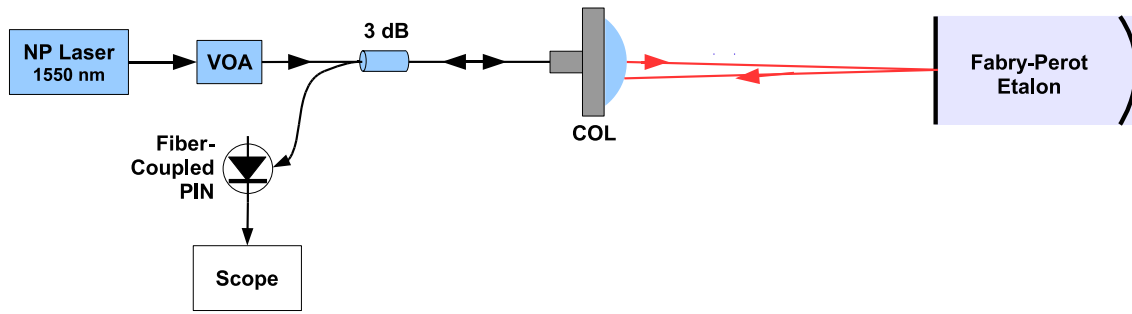
Fig. 7.1: Free-Space Optical Alignment

a 10% reflection at the cavity mirrors. Using the 1310 nm laser, the reflected signal contained components reflected from each mirror, and the input collimator position was adjusted to maximize the reflecion received by PIN1, thus fully establishing the optical axis. This beam was also used to adjust the position of PIN2 at the back of the vacuum chamber, which picks up the light transmitted through the etalon.

7.1.2   Modematching to the Etalon

Reconnecting the NP laser (1550 nm) and using the temperature tuning function to sweep the frequency over a 2 GHz range revealed over 10 resonant frequencies of the etalon. These partial resonances were indicated by small peaks in the transmitted signal, accompanied by partial nulls in the reflected signal. Since the FSR was calculated to be only 1.5 GHz, these results indicate that there were many higher-order Hermite-Gaussian modes present, each one with a different resonant frequency. Closer observation showed that the modes seen all had relatively equal power, a clear indication of the need for modematching lenses.

The polarizer, EOM, and modematching lenses were added to the path one at a time, and their positions and angles were tuned to maximize the reflected signal and maintain a clear set of partial resonances. With all of the components in place, small, final adjustments were necessary to complete the modematching process. The primary difficulty in this step

was choosing the correct resonant frequency to use as a reference. Attempting to maximize the transmission of a higher-order resonance only results in an incorrect alignment, because alignment errors are the primary cause of these higher order modes [17].

Through extensive experimentation, the fundamental mode was located, and the AOM was used to sweep the frequency of the input laser across a narrow bandwidth containing the resonance. The position and orientation of the modematching lenses were fine-tuned to achieve the best possible resonance, shown in Figure 7.2.
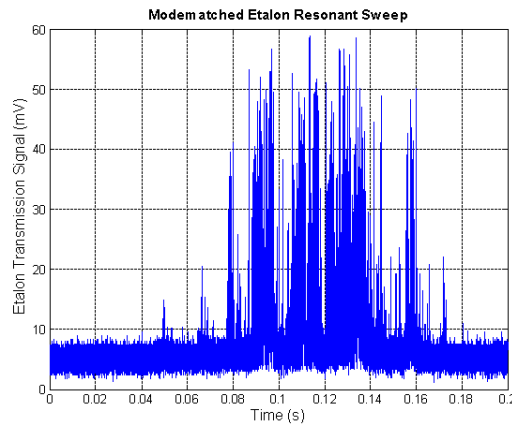
Fig. 7.2: Modematched Etalon Resonant Sweep

As the AOM swept the frequency of the incident light across the etalon resonance at a rate of 1.2 MHz/s, the un-stabilized input laser was generating a small amount of frequency noise. This frequency jitter is dominant in the transmission signal of Figure 7.2, which illustrates the extremely high sensitivity of the etalon. Even small, momentary drifts in input frequency can cause the constructive interference inside the high-finesse cavity to temporarily break down, generating a very noisy resonance curve. Despite the effects of frequency noise, Figure 7.2 shows good resonant transmission through the cavity and indicates that loss due to mode-mismatch is low.

7.2   Laser Frequency Locking

7.2.1   Reflection Spectrum and Modulation Depth

After modematching the incident light to the etalon geometry, the next step was to generate the Pound-Drever-Hall error signal. The EOM was powered on with an $\Omega = 10\ MHz$ RF input, and the AOM was used to center the frequency of the input laser near to the cavity resonance. The calculated spectrum of the incident, phase modulated light is shown in Figure 7.3.
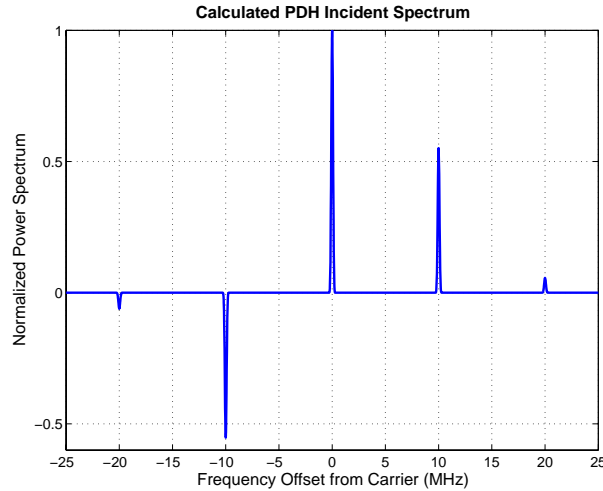
Fig. 7.3: Illustration of PDH Signal Reflection

The key aspect of the incident electric field spectrum is that the lower sidebands are 180° out of phase with the upper sidebands. If this signal, I_{inc}, were measured with a photodiode, several beat notes would form as a result of mixing between the sidebands. Due to the phase inversion, the beating between the upper sideband and the carrier would be canceled by the beating between the carrier and the lower sideband. If all of the incident power is assumed to be contained in the carrier and first order sidebands (as in Equation 3.4), the beat signal at $\Omega = 10\ MHz$, completely vanishes.

From Figure 3.3, it is clear that the key to the PDH technique is the steep phase inversion in the reflection spectrum. With the center frequency of the incident light near resonance, the signal carrier experiences a 90° phase shift. Now, the carrier is in quadrature with each of the first order sidebands, and a significant beat note at $\Omega = 10\ MHz$ is generated (Section 3.2).

The measured beat spectrum (Figure 7.4) appears exactly as expected, with extremely clean beat beat notes at multiples of 10 MHz. The presence of a strong first-order beat note confirms that the FP etalon is performing well with regard to the phase of the reflection coefficient. The measurement was taken as an average of 100 spectra, and the strength of the 10 MHz note indicates that the incident light spent a significant amount of time very near resonance during the data acquisition.

Fig. 7.4: Measured PDH Beat Signal
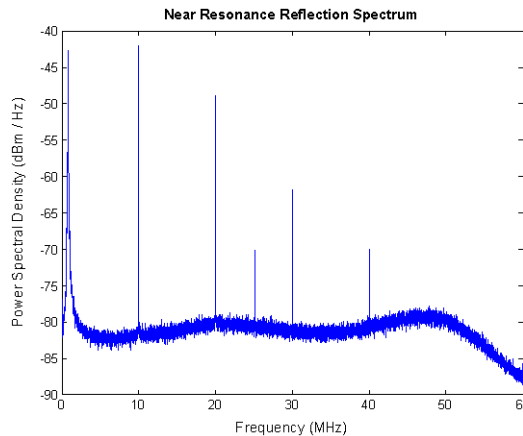
The strong, slightly wider peak at 880 kHz is the relaxation noise of the input laser, and not a part of the PDH modulation spectrum. This relaxation noise is due to spontaneous emission in the laser gain medium [30]. Its effect on the PDH system is negligible because its frequency is too low to interfere with the sidebands, and it is filtered out at the input of the receiver circuit.

7.2.2   The PDH Error Signal

The time-domain measurement of the reflected intensity provides a great deal of insight into the operation of the PDH system. With the EOM producing 10 MHz sidebands, the AOM was again used to move the laser center frequency almost exactly on resonance. Figure 7.5 shows the measured PDH error signal in the time domain. As the laser jitters back and forth across the resonant line, the carrier signal is partially reflected by the etalon, mixing with the sidebands to generate a 10 MHz beat note. At the instant that the carrier is exactly on resonance, its reflection is completely canceled, and the beat signal disappears. The graph clearly illustrates this phenomenon, where the envelope of the reflected signal is proportional to the instantaneous frequency error.
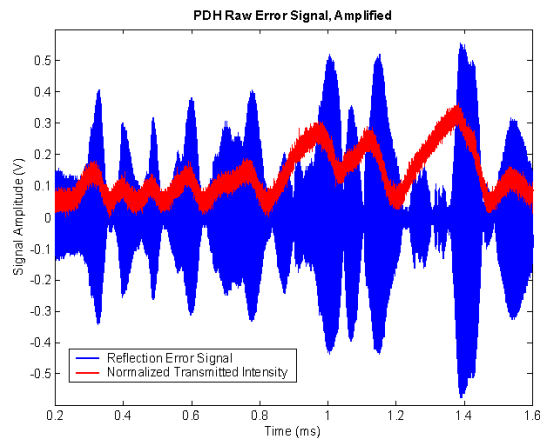
Fig. 7.5: Measured PDH Error Signal

In order to illustrate the properties of the FP etalon, the transmitted signal has also been included in Figure 7.5. Comparison between the two curves indicates the rationale behind the PDH scheme. The error signal is based on the reflection from the front of the etalon, where any quick changes in laser frequency have an instantaneous effect on the phase cancellation in the reflection. In contrast, the transmission signal is generated by the standing wave inside the cavity, which takes time to build up. This is why the transmitted

curve shows a smoothing effect, while the error signal curve provides real-time measurement of the incident frequency noise. The amplitude of the transmitted signal has been magnified in the curve to make it visible against the error signal.

After confirming that the system was generating the correct raw error signal, the next step was to test the downconversion and filtering process that would produce the final frequency error signal. With the laser frequency centered near resonance, the AOM was used to perform a narrow-band chirp of the input frequency across the etalon resonance at a rate of 600 kHz/s. A probe was used to measure the signal in the receiver circuit at the output of the mixer and lowpass filter elements. The result, shown in Figure 7.6 is a measurement of the final PDH error signal, which is fed directly to the VCO to cancel the frequency noise of the input laser.
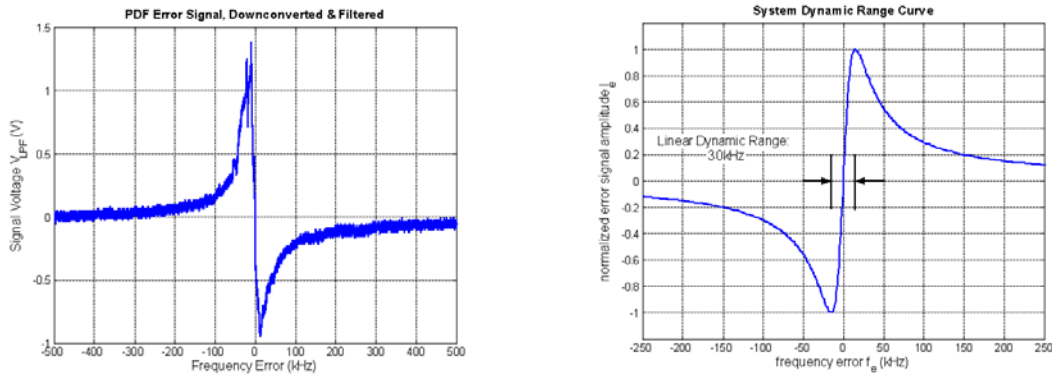
Fig. 7.6: Final PDH Error Signal, Measured

The similarities between the measured curve in Figure 7.6 and the calculated error signal in Figure 3.5 (reproduced here for reference) are striking. Most importantly, the linear dynamic range is measured to be about 25 kHz, very close to the predicted value of 30 kHz. The slight difference may be due to laser frequency noise (the input laser was not stabilized during this test) blurring the signal at the top and bottom ends of the range. Agreement between the two dynamic range values is a critical performance measurement

because it accurately indicates that the modematching system and FP cavity are working together correctly. The etalon is achieving its full potential finesse and producing a near-perfect error signal. The only other difference between the two graphs is the sign inversion in the measured curve, which is required to produce negative feedback.

7.3 Output Linewidth Estimation Technique

Measuring the final stabilized laser linewidth is more difficult than measuring the PDH sidebands and error signal. This section presents the challenges of accurate characterization of narrow linewidth lasers. An approximate solution is proposed to estimate the level of stabilization, and its implementation proves that the system provides a significant linewidth reduction.

7.3.1 Exact Linewidth Measurement

By far the simplest and most widely-used technique for measuring linewidth is Delayed Self-Heterodyne Interferometry (DSHI), in which the output of the laser under test is launched into a Mach-Zender interferometer (Figure 7.7). The incident light is allowed to beat with a time-delayed version of itself. For this technique to produce an accurate measurement, the delay line must be at least 6 times longer than the coherence length of the laser [31]. Related to the linewidth $\Delta\nu$ and group velocity of the fiber delay line v_g, the formula for coherence length L_c is given by Equation 7.1.

$$L_c = \frac{v_g}{\pi \Delta\nu} = \frac{c/n_{eff}}{\pi \Delta\nu} \tag{7.1}$$

Table 7.1 lists the coherence length and required delay lengths for DSHI measurement
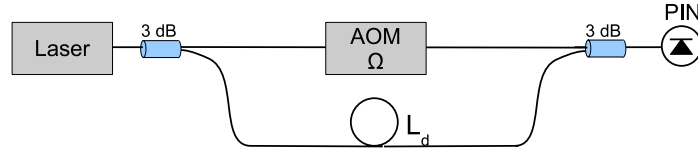
Fig. 7.7: DSHI Linewidth Measurement Setup

of several linewidths. The specifications are for Corning SMF-28 fiber, which has a group velocity of $v_g = 2.042x10^8 \ m/s$ at 1550 nm. It shows that the even the un-stabilized input laser, which has a linewidth of $1 - 2 \ kHz$, requires a Mach-Zender interferometer with a 390 km delay line to accurately measure its linewidth. Accurately characterizing the linewidth of the stabilized laser using this method would require an impossibly long fiber, or a huge recirculating loop [32].

Linewidth	Coherence Length	DSHI Length
$\Delta\nu$ (Hz)	L_c (km)	L_d (km)
1000	65	390
100	650	3,900
10	6,500	39,000
1	65,000	390,000

Tab. 7.1: Required Delay Length for DSHI Linewidth Measurement

Such a project would require a huge effort to thermally and mechanically isolate the recirculation loop to reduce Doppler broadening, and therefore is beyond the scope of this work. The commonly accepted alternative is the construction of a second Pound-Drever-Hall system to serve as a frequency reference [11, 14]. This is also not feasible. For these reasons, we attempt to simply demonstrate that the Pound-Drever-Hall system reduces the laser linewidth, and we leave a more exact characterization of the frequency stability for future work.

7.3.2   Sub-Coherence Length Linewidth Estimation

The coherence length limitation of DSHI makes it impractical for exact linewidth measurement of the stabilized laser, but under the right conditions, it can be used as a tool to roughly estimate the output linewidth and verify the system operation. If the DSHI technique is applied to a laser with $L_d < 6L_c$, the resulting beat spectrum generates a falsely narrow linewidth measurement [31]. As the interferometer length increases, the spectrum approaches the true laser linewidth. Equation 7.2 models frequency spectrum of the beat signal as a function of delay time τ_d.

$$
\begin{aligned}
S(\omega, \tau_d) &= \frac{P_0^2 \tau_c}{2\left[1 + (\omega \pm \Omega)^2 \tau_c^2\right]} \left\{ 1 - e^{-\tau_d/\tau_c}\left(\cos\left[(\omega \pm \Omega)\tau_d\right] + \frac{\sin\left[(\omega \pm \Omega)\tau_d\right]}{(\omega \pm \Omega)\tau_c} \right) \right\} \dots \\
&+ \frac{1}{2} P_0^2 \pi e^{-\tau_d/\tau_c} \delta(\omega \pm \Omega)
\end{aligned}
\tag{7.2}
$$

This expression assumes that the lineshape of the laser under test is Lorentzian. The Lorentzian spectrum is the canonical laser lineshape (Equation 7.3), arising from white frequency noise. As discussed in Chapter 5, the NP input laser has an unusual "pink" frequency noise spectrum, resulting in a Voigt lineshape. The Voigt profile is approximately equal to the convolution between the Lorentzian and Gaussian lineshapes [33], and for the purposes of this analysis, the Lorentzian distribution makes a reasonable illustrative approximation.

$$
S_{Lorentzian}(f) = \frac{1}{(\Delta\nu/2)^2 + f^2}
\tag{7.3}
$$

Figures 7.8 and 7.9 clearly depict the behavior of Equation 7.2 as it pertains to the NP Photonics input laser and Pound-Drever-Hall laser output. The proposed technique is simple: first, the linewidth of the un-stabilized input laser is measured with as long of a

delay line as possible ($L_d = 150 \ km$), producing the spectrum shown in Figure 7.8. For simulation purposes, the true lineshape of the input laser is assumed to be Lorentzian with $\Delta\nu = 1 \ kHz$ FWHM linewidth. In this case, $L_d \approx 2.9 L_c$, and the calculated DSHI beat note very closely resembles the true linewidth. Close inspection reveals a small amount of ripple and a narrow peak (due to the δ-function in Equation 7.2) at the center of the spectrum.
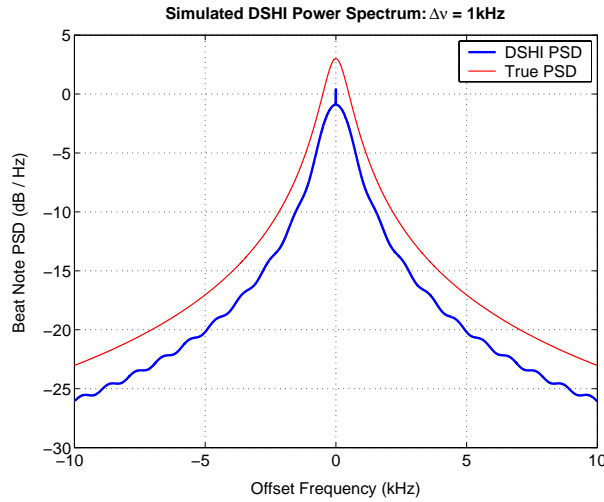

Fig. 7.8: Simulated DSHI Measurement of Input Laser

If the same Mach-Zender interferometer is used to measure the linewidth of the stabilized laser output, the delay length becomes much shorter than the coherence length, and the beat note spectrum changes dramatically. Figure 7.9 shows the simulated DSHI spectrum for a laser stabilized to 100 and 10 Hz linewidths. As the level of stability increases, the interferometer becomes less adequate to make an accurate measurement. The ripple becomes very dominant, the peak narrows, and the δ-function spike becomes more prominent.

These visual patterns are used in the next section to show that the Pound-Drever-Hall system does indeed provide a significant level of stabilization of the input laser. Although a true linewidth measurement is not attempted, the presence of the δ-function peak and narrowing of the overall spectrum is a good indicator of linewidth reduction.
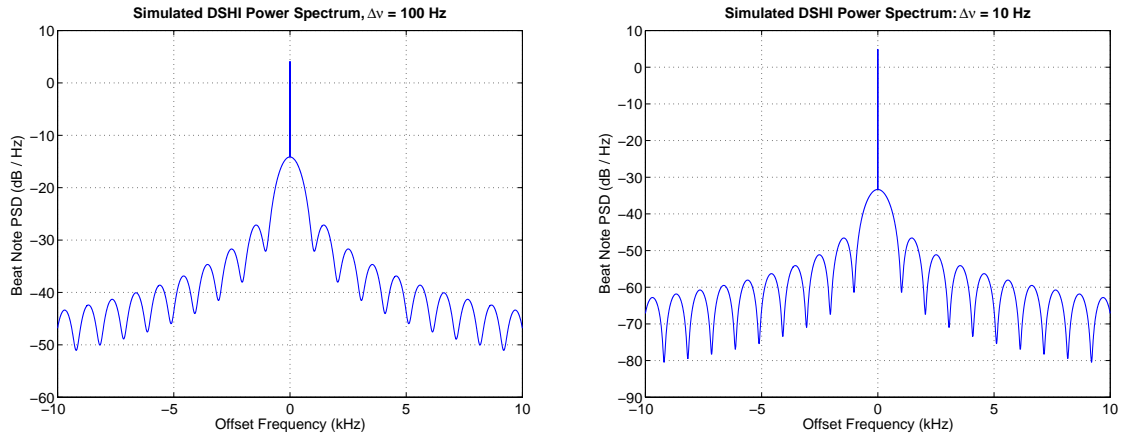
Fig. 7.9: Simulated DSHI Measurement of Stabilized Output

7.4   *Stabilized Linewidth Results*

The sub-coherence length DSHI setup used to estimate the stabilized linewidth is nearly identical to the one depicted in Figure 7.7. Six Corning SMF-28 fiber spools were connected in series to form the loop, and an Erbium Doped Fiber Amplifier (EDFA) was added to the middle of the loop to compensate for the 5 $dB/spool$ loss. The AOM in the short arm of the interferometer produces a 37 MHz frequency shift, and the beat note was measured with a high-speed amplified photodiode.

Environmental isolation for the fiber spools was provided by a large cabinet lined with 4" of foam. Thermal and mechanical stabilization of the loop is critical to measurement accuracy due to the extremely long path length. Any thermal fluctuations can cause changes in both the refractive index and physical length of the fiber, altering the OPL. These time-varying changes in path length induce a Doppler shift in the light, effectively broadening the measured linewidth. Acoustic waves coupled into the fibers can also cause Doppler broadening.

In addition to environmental sources, the measurement accuracy is also limited by

nonlinear effects in the fiber. The main cause of nonlinear spectral broadening in silica fiber is stimulated Brillouin scattering, which can be ignored if the intensity is below a threshold of about 2 mW [32]. Placing the EDFA in the middle of the loop minimizes the peak amplified intensity, which is kept below the Brillouin threshold value.

The accuracy of this measurement relies on the fact that both the stabilized and un-stabilized lasers interact with the same noise sources during linewidth measurement. Comparison between the two spectra is unaffected by any consistent noise source. Given that the two measurements were taken in succession, it is reasonable to assume that both measurements display similar levels of noise-induced broadening.

During the testing procedure, it was discovered that the PDH system was not capable of maintaining a frequency lock for more than 6 seconds at a time. The linewidth estimation procedure was designed with this limitation in mind. With the PDH electronics disconnected, the input laser was allowed to "run free", and the output linewidth was measured. Then, the frequency locking electronics were powered on, and the AOM center frequency was manually adjusted to bring the free-running laser into locking range. Linewidth data for the stabilized laser was then collected and stored before the system lost its lock. This procedure was repeated 16 times.

Data was acquired using a digital oscilloscope to sample the beat note at $f_s = 100\ MHz$ for $\tau = 2.0\ ms$. The FFT power spectrum of each acquisition was calculated using Welch's method, and the 16 separate acquisitions were averaged to produce the final spectra for both the stabilized and un-stabilized laser signals. Figure 7.10 shows the final comparison between the beat spectra of the two signals.

The two curves clearly show that the Pound-Drever-Hall system significantly improves the frequency stability of the input laser. The stabilized linewidth is much narrower than
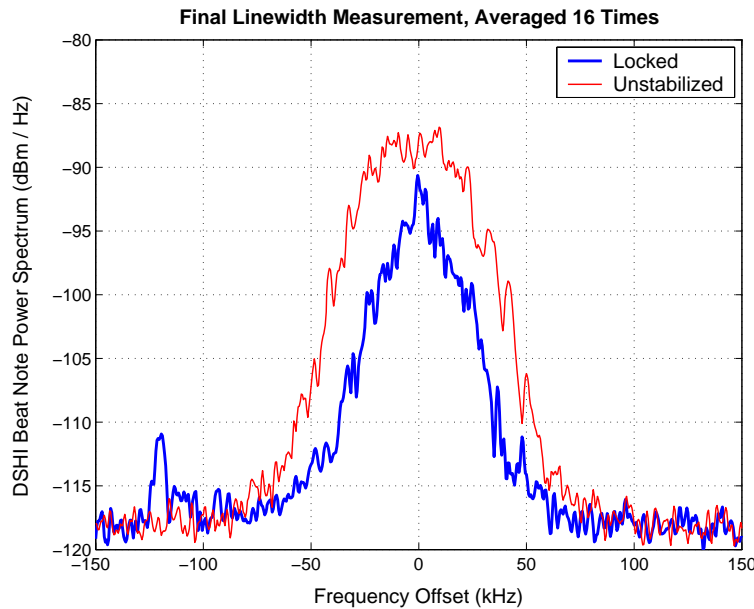
Final Linewidth Measurement, Averaged 16 Times

Fig. 7.10: Final Linewidth Measurement Results

the input laser linewidth throughout the entire spectrum, and it also displays a small peak a the top of the curve. This peak is the measured equivalent of the δ-function in the calculated DSHI spectra (Figure 7.9), and due to the FFT resolution limitation of $df = 500 \ Hz$, the actual spectrum may have an even stronger, narrower peak than shown in Figure 7.10. This is a strong indication that the coherence length of the stabilized laser is significantly longer than $150 \ km$.

Neither curve has a Lorentzian spectrum, an indication of the flicker noise dominance of the input laser, which introduces a Gaussian component to the lineshape. The broad spectral width of the curves is partially due to environmental and nonlinear noise, but the averaging method is not appropriate for making an estimate of actual linewidth. Figure 7.9 is essentially a series of short-term linewidth snapshots, taken over a duration of several minutes and then averaged. As a comparative tool, however, it proves that the PDH system works properly in the case of short-term ($2 \ ms$) linewidth stabilization.

8. DISCUSSION

8.1   Statement of Results

The goal of this project was to design and build a working Pound-Drever-Hall frequency locking system and demonstrate that it improves the frequency stability of a narrow-linewidth laser source. Throughout the design and assembly process, each component of the system was individually tested for basic operation and noise performance. During the final system assembly, several tests were performed to verify the generation of a proper PDH error signal. The final linewidth measurement was made using the sub-coherence length DSHI technique, and then comparing the data from the stabilized and un-stabilized lasers. The results are clear: the PDH system significantly reduces the short-term linewidth of the input laser.

Due to dynamic range issues, the Continuous Wave (CW) output of the PDH frequency locking system is limited to a duration of approximately 6 seconds before the locking electronics must be re-adjusted. This is more than sufficient for most heterodyne experiments, and with its output power of about 1 mW, the stabilized laser system can be used for a variety of applications from sensor characterization to linewidth measurement.

8.2 Future Work

The promise of future development was a major factor throughout the design process. Whenever possible, each critical piece of the system was built to achieve the highest level of performance with only a few simple alterations. The vacuum chamber, for example, was designed to meet Ultra-High-Vacuum (UHV) tolerances, and it was built with extra connections for turbomolecular and ion vacuum pumps. With this small bolt-on modification, the chamber would be able to maintain a vacuum at the 10^{-11} *torr* level.

Further experimentation with the filter and gain elements in the receiver circuit could be used to optimize and fine-tune the system performance. Although direct measurement of the modulation depth is difficult, fine adjustments of the RF input power to the EOM could be made to optimize the phase modulation depth. The addition of a second, low-finesse "pre-locking" loop has also been considered to remedy the dynamic range problems and produce a long-term CW output. Such a loop would require additional modifications and optimization of the electronic control loop parameters to make the two feedback loops work together properly.

Although the temperature control system has reached an extremely high level of stability, the acoustic, mechanical, and vacuum stabilization systems have room for improvement. As discussed previously, improving the quality of the vacuum simply involves the addition of several UHV pumps. As for mechanical stabilization, many engineers have gone through considerable lengths to reduce the natural vibrational frequency of their PDH systems [4, 11, 14]. Improvements may include a move to a more stable, basement laboratory environment and the construction of a more massive, active mechanical stabilization system. A more specialized acoustic foam could be used in the enclosure, and the external lab environment could also be acoustically isolated.

The final suggestion for future work lies in the realm of linewidth measurement. Efforts are already underway to make a more accurate characterization of the output frequency stability. Many of the challenges to the DSHI technique are similar in nature to the mechanical stabilization issues of the PDH system, so the linewidth estimation setup could benefit from similar environmental isolation improvements. Other measurements could also be made, such as a time-domain phase noise measurement, and a direct characterization of the output frequency noise spectrum. Ultimately, to fully characterize the output frequency stability, a second PDH system must be constructed.

BIBLIOGRAPHY

[1] R. W. P. Drever and J. L. Hall. Laser phase and frequency stabilization using an optical resonator. *Applied Physics B.*, 31:97, 1983.

[2] B. C. Young et al. HG+ optical frequency standard: Recent progress. In *International Conference on Laser Spectroscopy*, June 1999.

[3] M. A. Lombardi. *NIST Frequency Measurement and Analysis System: Operator's Manual*, 2001. Appendix A: An Introduction to Frequency Calibrations.

[4] M. Zhu and J. L. Hall. Short and long term stability of optical oscillators. In *IEEE Frequency Control Symposium*, page 44, 1992.

[5] L. Hollberg. Optical frequency / wavelength references. *Journal of Physics B*, 38:S469, 2005.

[6] S. A. Webster, M. Oxborrow, and P. Gill. Subhertz-linewidth Nd:YAG laser. *Optics Letters*, 29(13):1497, 2004.

[7] R. L. Barger, M. S. Sorem, and J. L Hall. Frequency stabilization of a cw dye laser. *Applied Physics Letters*, 22(11):573, 1973.

[8] A. Czajkowski, J. E. Bernard, A. A. Madej, and R. S. Windeler. Absolute frequency measurement of acetylene transitions in the region of 1540 nm. *Applied Physics B*, 79:45, 2004.

[9] C. Svelto. Frequency stability measurements of 1.5 μm erbium lasers locked to acetylene absorption lines. *IEEE Transactions on Instrumentation and Measurement*, 48(2):537, 1999.

[10] Ch. Spielberg et al. Compact 100 mw fiber laser with 2 khz linewdith. In *Optical Fiber Communications Conference*, volume 3, pages PD45–1, 2003.

[11] B. C. Young, F. C. Cruz, W. M. Itano, and J. C. Bergquist. Visible lasers with subhertz linewidths. *Physical Review Letters*, 82(19):3799, 1999.

[12] G. Hernandez. *Fabry-Perot Interferometers*. Cambridge, 1988.

[13] Eric D. Black. An introduction to pound-drever-hall laser frequency stabilization. *American Journal of Physics*, 69(1):79, 2000.

[14] M. Roberts, P. Taylor, and P. Gill. Laser linewidth at the sub-hertz level. Technical Report CLM 8, National Physics Laboratory, U.K., 1999.

[15] A. Yariv. *Quantum Electronics*. Wiley, 1989.

[16] D. Marcuse. Loss analysis of single-mode fiber splices. *Bell Systems Technical Journal*, 56:703–719, 1977.

[17] H. Kogelnik. Coupling and conversion coefficients for optical modes. In *Proceedings of the Symposium on Quasi-Optics*, pages 333–347. Polytechnic Institute of Brooklyn, 1964.

[18] J. L. Hall, J. Ye, and L. S. Ma. Measurement of mirror birefringence at the sub-ppm level: Proposed application to a test of QED. *Physical Review A*, 62(1):013815, 2000.

[19] J. Lekavich. Basics of acousto-optic devices. *Lasers and Applications*, page 59, April 1986.

[20] M. Gardner. Mathematical games: White and brown music, fractal curves and one-over-f fluctuations. *Scientific American*, 238(4):16–32, 1978.

[21] P. D. Welch. The use of fast Fourier transform for the estimation of power spectra: A method based on time averaging over short, modified periodograms. *IEEE Transactions on Audio and Electroacoustics*, 15(2):70, 1967.

[22] J. C. Bergquist, W. M. Itano, and D. J. Wineland. Laser stabilization to a single ion. In *Frontiers in Laser Spectroscopy*, Proceedings of the International School of Physics (Enrico Fermi), pages 359–376, 1994.

[23] Newport Corp. *I-2000 LabLegs Datasheet*.

[24] B. Hardin. The nature of damping in sands. *Journal of the Soil Mechanics and Foundations Division, Proceedings of the ASCE*, 91(1):63–97, 1965.

[25] G. Ballou, editor. *Handbook for Sound Engineers*. Focal Press, 1998.

[26] J.W. Berthold III and S.F. Jacobs. Ultraprecise thermal expansion measurement of seven low expansion materials. *Applied Optics*, 15(10):2344, 1976.

[27] Macklen, editor. *Thermistors*. Electrochemical Publications, 1979.

[28] D. W. Clarke. PID algorithms and their computer implementation. *Transactions of the Institute of Measurement and Control*, 6(6):305, 1984.

[29] Michael F. Modest. *Radiative Heat Transfer*. Academic Press, 2003.

[30] C. H. Henry. Theory of the phase noise and power spectrum of a single mode injection laser. *IEEE Journal of Quantum Electronics*, 19(9):1391–1397, 1983.

[31] L. E. Richter et al. Linewidth determination from self-heterodyne measurements with subcoherence delay times. *IEEE Journal of Quantum Electronics Letters*, 22(11):2070–2074, 1986.

[32] X. Chen. *Ultra-Narrow Laser Linewidth Measurement*. PhD thesis, Virginia Tech, 2006.

[33] L. B. Mercer. 1/f frequency noise effects on self-heterodyne linewidth measurements. *Journal of Lightwave Technology*, 9(4):485–493, 1991.

APPENDIX

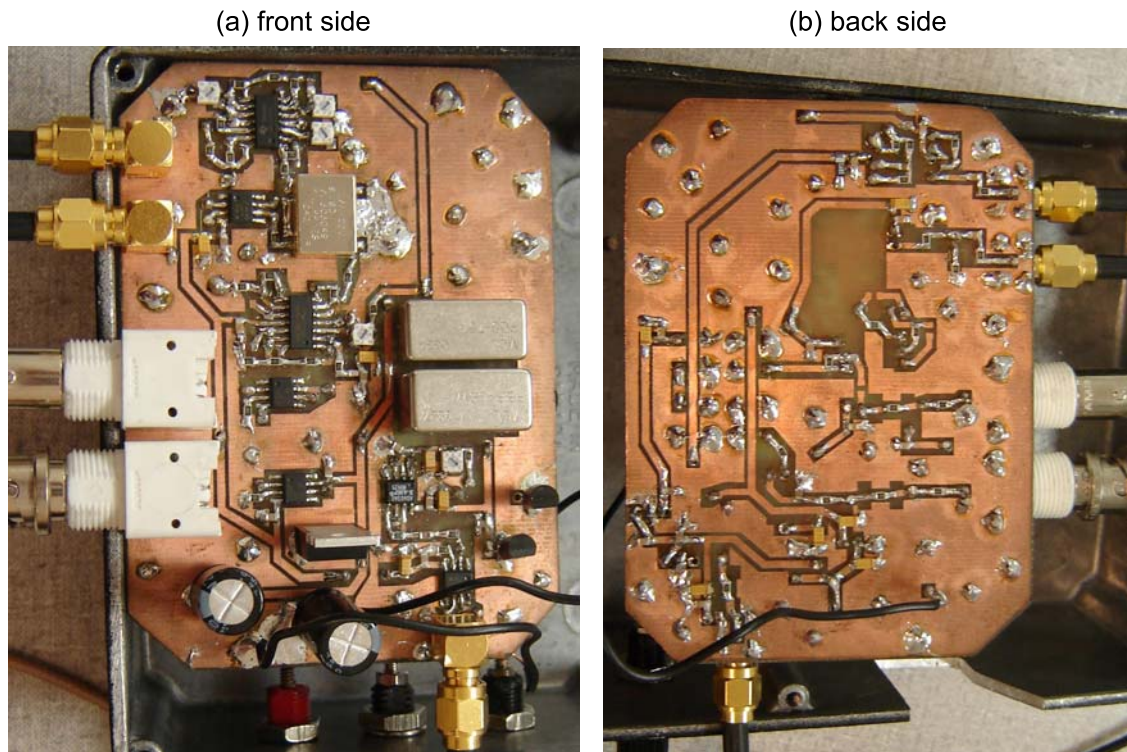# A. PHOTOGRAPHS
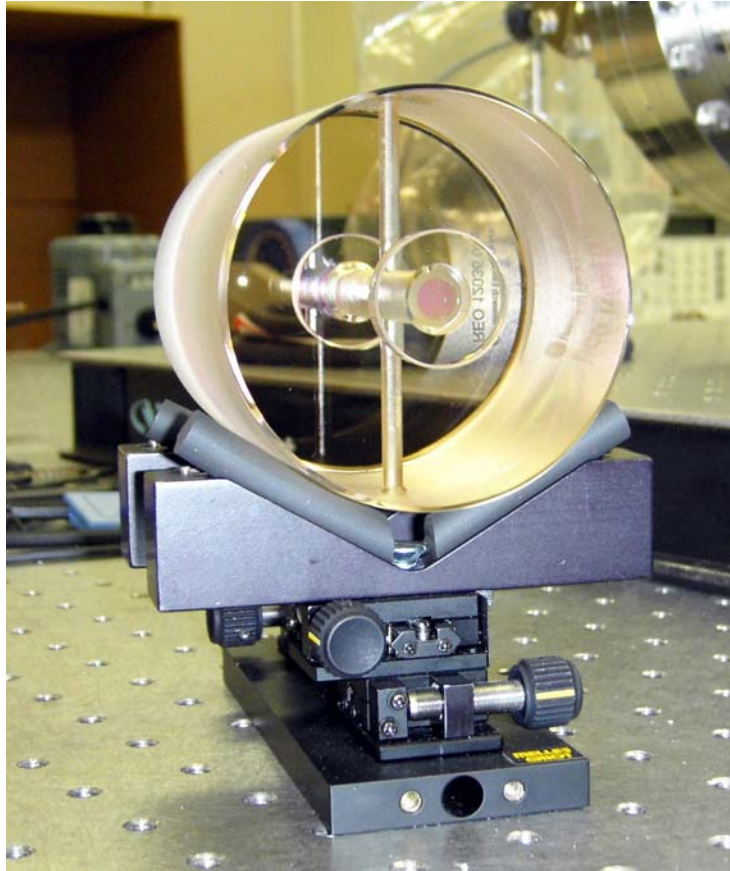
Fig. A.1: Fabry-Perot Etalon on its Mount

(a) front side   (b) back side
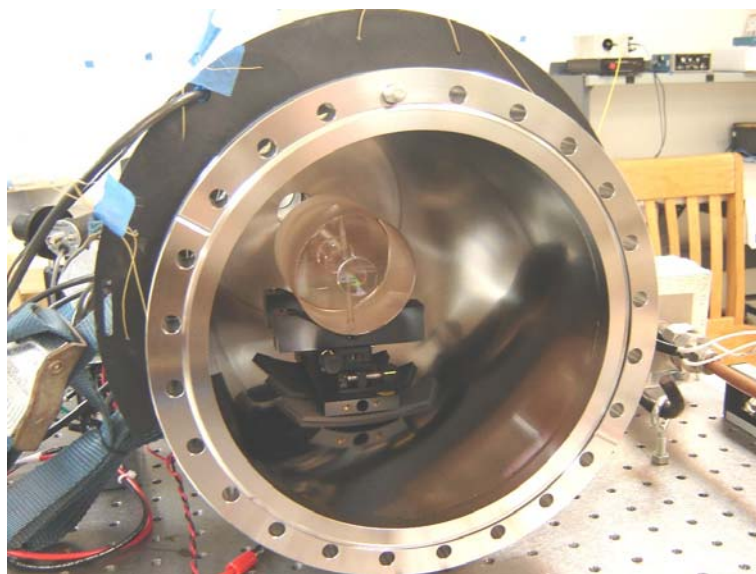

Fig. A.2: Finished Receiver Circuit

Fig. A.3: Fabry-Perot Etalon in Vacuum Chamber

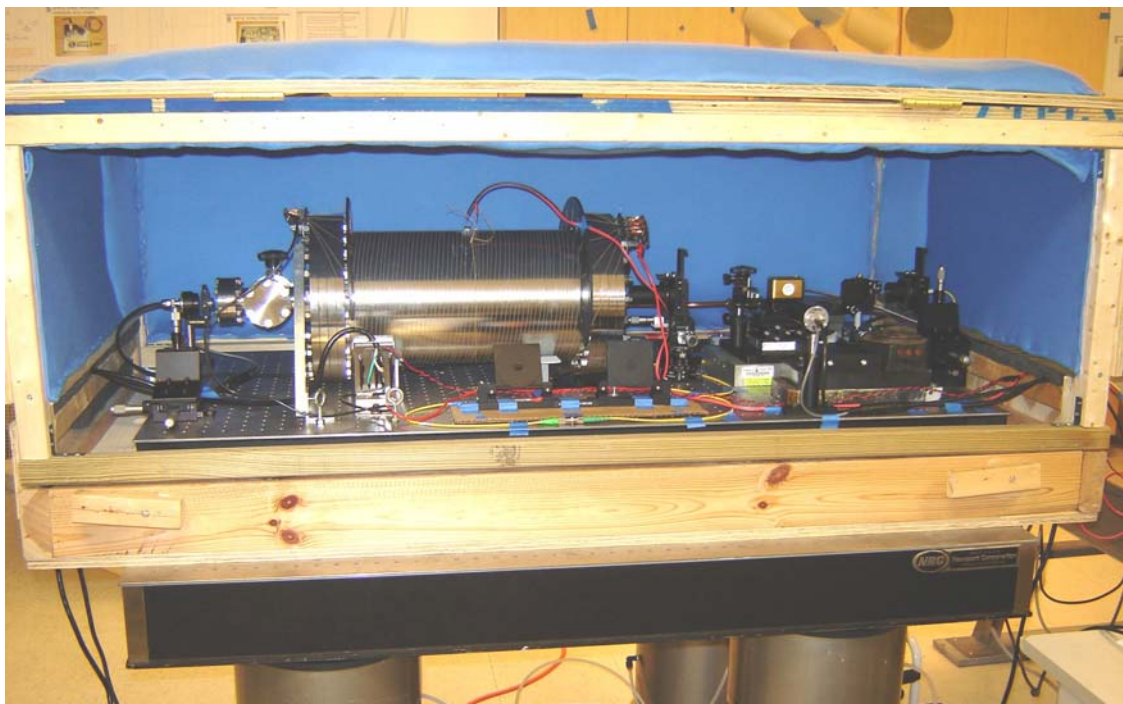*Fig. A.4:* Sandbox and Acoustic Enclosure
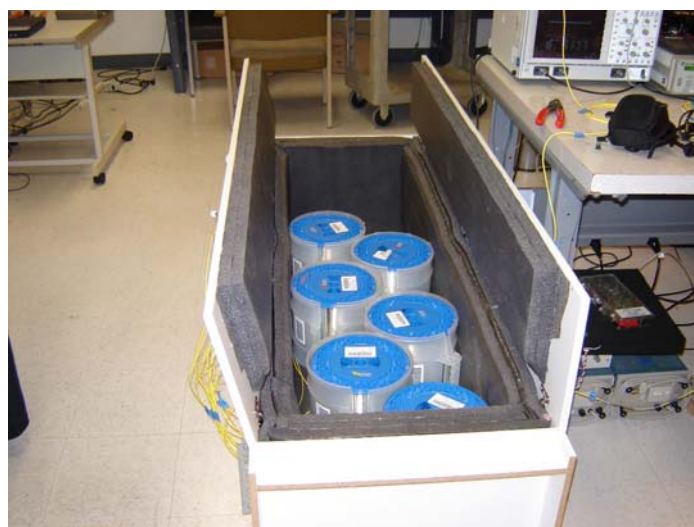

Fig. A.5: PDH System (View 1)

Fig. A.6: PDH System (View 2)

Fig. A.7: DSHI Linewidth Measurement Loop